ARTICLE IN PRESS

Nano Materials Science xxx (xxxx) xxx

Contents lists available at ScienceDirect

Nano Materials Science

journal homepage: www.keaipublishing.com/cn/journals/nano-materials-science/

Time-/environment-dependent multilevel optical encryption through photoluminescence enhancement of perovskite quantum dot/polymer composite *via* silver epoxy paste

Jaehyeok Ryu [a], Jiyeon Lee [a], Dongjun Kim [a], Yu Jin Lee [b], Ji Heon Kim [c], Juwon Oh [c], Jiwon Kim [a,d,e,*]

[a] *School of Integrated Technology, College of Computing, Yonsei University, 85 Songdogwahak-ro, Yeonsu-gu, Incheon 21983, Republic of Korea*
[b] *Department of Chemistry, College of Science, Yonsei University, 50 Yonsei-ro, Seodaemun-gu, Seoul 03722, Republic of Korea*
[c] *Department of Chemistry, College of Natural Science, Kyungpook National University, 80 Daehak-ro, Buk-gu, Daegu 41566, Republic of Korea*
[d] *Integrated Science and Engineering Division, Underwood International College, Yonsei University, 85 Songdogwahak-ro, Yeonsu-gu, Incheon 21983, Republic of Korea*
[e] *Department of Integrative Biotechnology, Graduate School, Yonsei University, 85 Songdogwahak-ro, Yeonsu-gu, Incheon 21983, Republic of Korea*

ARTICLE INFO

Keywords:
Perovskite quantum dot/polymer nanocomposite
Silver epoxy paste
Photoluminescence
Surface defect passivation
Diffusion
Optical encryption

ABSTRACT

Perovskite quantum dot (PQD)/polymer nanocomposites have garnered significant attention in the field of advanced optical encryption due to their eminent photoluminescence (PL) properties and stability. Nonetheless, the strategies introduced often necessitate sophisticated experimental setup, presenting challenges for the practical application. Herein, we have designed a time/environment-dependent optical encryption methodology which leverages the PL enhancement of cesium lead bromide ($CsPbBr_3$) PQD/polydimethylsiloxane (PDMS) film through the application of silver (Ag) epoxy paste (AEP). Following heat treatment under vacuum after AEP application on the film surface, diffused Ag^+ ions efficiently passivated the surface defects of $CsPbBr_3$ PQDs, leading to an enhanced quantum yield of 20.7 %. AEP treatment was further exploited as a multilevel encryption technique by modulating the treatment and environmental conditions. Encrypted information was initially concealed under daylight and masked by fictitious information under UV light. This information was decrypted over time, exhibiting variances in PL intensity as quenching progresses. To prevent information leakage, the decrypted information could be reverted to the fictitious information *via* a rapid quenching of the AEP-treated film in aqueous environment. This research not only paves a new pathway toward an efficient defect passivation strategy for PQDs but also advances a straightforward, yet sophisticated optical encryption strategy.

1. Introduction

In an increasingly digital and interconnected environment, a substantial volume of information is conveyed and received across various channels. In parallel with anticounterfeiting, the advancement of information encryption emerges as a crucial mechanism for protecting data integrity, privacy preservation, adherence to regulatory standards, and safeguarding against a spectrum of security vulnerabilities in information dissemination [1]. The growing requirement for sophisticated levels of security in information encryption has propelled research into multilevel optical encryption technologies utilizing functional materials [2,3].

Specifically, recent investigations have explored the potential of optical encryption methodologies employing photoluminescent (PL) materials by modulating their optical and physical characteristics (*e.g.*, PL intensity, photon lifetime, and crystal structure) [4–6]. This included the development of conjugated PL systems through the amalgamation of fluorescent materials with anti-Stokes fluorescent and/or phosphorescent materials [7–11], and the application of multi-stimuli (*e.g.*, thermal and chemical reagents) responsive fluorescent materials [12,13].

Among the diverse array of fluorescent materials, cesium lead halide ($CsPbX_3$; X = Cl, Br, I) perovskite quantum dots (PQDs) stand out for their excellent PL properties upon ultraviolet (UV) light irradiation characterized by high color purity, narrow emission band, defect tolerance and high photoluminescence quantum yields (PLQY) [14–16]. Nonetheless, their

---

* Corresponding author. School of Integrated Technology, College of Computing, Yonsei University, 85 Songdogwahak-ro, Yeonsu-gu, Incheon 21983, Republic of Korea.

E-mail address: jiwon.kim@yonsei.ac.kr (J. Kim).

Peer review under the responsibility of Chongqing University

https://doi.org/10.1016/j.nanoms.2025.03.004

2589-9651/© 2025 The Author(s). Publishing services by Elsevier B.V. on behalf of KeAi Communications Co. Ltd. This is an open access article under the CC BY-NC-ND license (http://creativecommons.org/licenses/by-nc-nd/4.0/).

Please cite this article as: J. Ryu et al., Time-/environment-dependent multilevel optical encryption through photoluminescence enhancement of perovskite quantum dot/polymer composite *via* silver epoxy paste, Nano Materials Science , https://doi.org/10.1016/j.nanoms.2025.03.004

susceptibility to an external conditions (*e.g.*, thermal exposure, moisture, and oxygen) often limits their application in optical encryption, as well as in light emitting diodes (LEDs), solar cells, and photodetectors [17].

Incorporating $CsPbX_3$ PQDs within polymer matrices affords a degree of isolation and protection from external environments, thereby enhancing stability. The entangled structure of polymer shields PQDs from external influences while allowing for controlled interactions (*e.g.*, swelling-deswelling of polymer matrix [13] and ion migration through the free volumes in polymer matrix [18]). Consequently, PQD/polymer nanocomposites facilitate the creation of a stable, external-stimuli-responsive optical encryption system. For instance, Wang et al. [13] devised an encryption/decryption method predicated on the PL quenching of $CsPbBr_3$ PQD/polyvinylidene fluoride (PVDF) nanocomposite *via* a swelling-deswelling process in a mixed solvent of water and N,N-dimethylformamide (DMF). Similarly, Wu et al. [19] endowed $CsPbX_3$ PQDs encapsulated within magnesium silicate hollow spheres (MSHSs) with hydrochromic properties through Cd^{2+} metal ion doping, enabling a stable and reversible encryption/decryption processes *via* humidification/dehumidification cycles.

While the aforementioned encryption strategies predominantly utilized a binary PL ON/OFF approach, few studies have explored multilevel optical encryption methods using PQD/polymer nanocomposites. Fu et al. [5] patterned $CsPbBr_3$ PQD/polycarbonate (PC) nanocomposite film by degrading PQDs with a laser at various power levels, enabling decryption through the passivation of surface defects *via* water infiltration into the polymer matrix. Liu et al. [18] achieved spatiotemporally tunable optical encryption with multiple levels by inducing gradient color changes in PQD/PDMS composite *via* halide ion exchange during solvent immersion process. Nevertheless, these advanced multilevel optical encryption strategies often necessitate complex synthesis process, sophisticated instrumentation, and toxic solvents such as hexane and dimethylformamide (DMF), which limit their practical applicability.

Meanwhile, the optoelectrical and physical properties of PQDs can be further enhanced through metal ion incorporation. This approach includes bandgap energy regulation by alloying perovskites with metal ions or morphological adjustment of perovskites (*e.g.*, grain size) by removing metal ions during crystallization [20–22]. Also, doping with metal ions (Ag^+, Mn^{2+}, Zn^{2+}, Cd^{2+}, Co^{2+}) [23–26] as a mean to augment optical efficiency *via* defect passivation has garnered significant attention for PQDs, given that surface defects can act as traps for non-radiative recombination centers, thereby lowering stability and PLQY [27]. Notably, post-synthesis doping methods have been explored for their simplicity relative to *in situ* metal ion integration during synthesis [28–30]. Nevertheless, these methods still face challenges, including limited solution process and supplementary equipment requirements.

Herein, silver (Ag) epoxy paste (AEP) treatment is introduced as a facile post-synthesis doping approach for passivating surface defects in $CsPbBr_3$ PQD/poly(dimethylsiloxane) (PDMS) film, facilitated as a straightforward, yet advanced multilevel optical encryption strategy. AEP, an adhesive comprising silver particles and ions, is widely employed in the electronics industry to foster electrical conductivity. In the AEP treatment process, this paste was applied to the surface of the film, which subsequently underwent thermal treatment under vacuum. Ag^+ ions from the paste permeated the PDMS matrix *via* free volumes which efficiently passivate surface vacancy defects on $CsPbBr_3$ PQDs, leading to pronounced enhancements in PL properties (*e.g.*, intensity, lifetime, and PLQY). By precisely regulating the treatment and external environmental conditions, AEP treatment was further utilized as a time-responsive multilevel encryption method *via* disparities in the PL quenching rates across each pattern, subjected to the specific conditions of AEP treatment. Specifically, an encrypted information remained concealed under daylight and was initially masked by a spurious pattern exhibiting green emissive fluorescence under UV light. Moreover, the strategic introduction of a trace amount of water facilitated an inversion in the PL intensity between the patterned and unpatterned regions of the film. Leveraging these methodologies, a time- and environment-dependent multilevel optical encryption framework was designed. This approach facilitates a gradual decryption of encrypted information under UV light, safeguarding the decrypted data by irreversibly reverting it to the original fake pattern through subsequent immersion in water followed by full decryption. This exposition underscores the potential of AEP treatment for implementing a multilevel optical encryption strategy, offering a pragmatic and economical solution.

2. Materials and Methods

2.1. Materials

$PbBr_2$ ($\geq$98 %), Cs_2CO_3 (99.9 %), oleic acid (OA) (90 %), octadecene (ODE) (90 %), and oleylamine (OAm) (70 %) were purchased from Sigma-Aldrich. Acetone (99.5 %) and *n*-hexane (95 %) were sourced from Samchun and Daejung, respectively. Sylgard 184 elastomer kit was purchased from Dow Chemical, and Silver conductive epoxy adhesive (AEP) composed of part A and B (8331S-15G 4hr) was purchased from Mg Chemical.

2.2. Preparation of $CsPbBr_3$ PQDs

2.2.1. Synthesis of Cs-oleate

Cs_2CO_3 (0.814 g, 2.5 mmol) was dissolved in a mixture of OA (2.5 mL) and ODE (40 mL) in a 100 mL three-neck round bottom flask, followed by degassing at 120 °C under vacuum for 1 h. Subsequently, the reaction between OA and Cs_2CO_3 was progressed under N_2 gas by heating up to 150 °C and cooled down to room temperature (RT) after the reaction. Cs-oleate was preheated to 140 °C before the injection.

2.2.2. Synthesis of $CsPbBr_3$ PQDs

$PbBr_2$ (0.69 g, 1.88 mmol) dissolved in a mixture of ODE, OAm, and OA in a volume ratio of 50:8:8 (mL) was heated to 120 °C, evacuated, and refilled with N_2 gas. Once the temperature reached 120 °C, the solution was vigorously stirred for 1 h. Next, 5 mL of preheated Cs-oleate was quickly injected and reacted with $PbBr_2$ precursor for 1 min. The mixture was then rapidly quenched in an ice-water bath. Quenched solution containing $CsPbBr_3$ PQDs was centrifuged at 8000 rpm for 10 min, and the supernatant was discarded followed by particle redispersion in *n*-hexane for storage. Synthesized $CsPbBr_3$ PQDs were precipitated with acetone to wash the excess ligands, and centrifugation was conducted for 10 min at 8000 rpm, followed by redispersion in *n*-hexane.

2.3. Synthesis of $CsPbBr_3$ PQD/PDMS film

Here, 1 g of PDMS was mixed with 0.1 g of curing agent under stirring. Next, 1 mL of purified $CsPbBr_3$ PQDs dissolved in *n*-hexane was added dropwise (1 droplet/5 s) under vigorous stirring (400 rpm to 500 rpm) and stirred for additional 10 min to 30 min $CsPbBr_3$ PQD/PDMS prepolymer was vacuumed for 1 h to 2 h to remove *n*-hexane and poured into a flat-bottomed plastic Petri dish to form $CsPbBr_3$ PQD/PDMS film, followed by vacuum curing at 60 °C for 6 h using a vacuum oven.

2.4. Ag^+ ion doping into $CsPbBr_3$ PQD/PDMS film via AEP treatment

Parts A and B of AEP were mixed in a volume ratio of 1:1. The mixed AEP was then applied to the surface of $CsPbBr_3$ PQD/PDMS film and cured for several hours under vacuum at various temperatures. After the heat treatment, AEP was removed by a repetitive peeling with a tape on the film's surface.

2.5. Compositional characterization

The physical properties of the films were measured using an Fourier transform infrared spectrometer (FT-IR spectrometer; Cary670, Agilent, USA). The surface morphology was analyzed by water contact measurements with a tensiometer (OCA 15 EC, DataPhysics Instruments, Germany) and atomic force microscope (AFM; NX-10, Park Systems, Korea). Topographical imaging was obtained using AFM in tapping mode with a frequency of 160–220 kHz and a spring constant of 27–71 N/m. Thin film X-ray diffraction patterns were obtained *via* high resolution X-ray diffraction system (HR-XRD; SmartLab, Rigaku, Japan) with Cu Kα radiation. The chemical composition of AEP-treated $CsPbBr_3$ PQD/PDMS film was investigated using Inductively coupled plasma-mass spectrometer (ICP-MS; 7900, Agilent, USA), X-ray fluorescence spectrometer (XRF; ZSX Primus, Rigaku, Japan), and X-ray photoelectron spectrometer (XPS; K-Alpha, Thermo Scientific, USA). For liquid phase ICP-MS analysis, sample solutions were prepared by immersing sliced film (10×5 mm^2) in 2 mL of Ag etchant solution until they completely decomposed into Cs, Pb, Br, and Ag. The surface morphology and elemental composition were obtained using focused ion beam field-emission scanning electron microscope (FIB-FE-SEM; JIB-4601F, JEOL, Japan) with electron energy dispersive spectroscopy (EDS) mapping and time-of-flight secondary ion mass spectrometer (TOF-SIMS; TOF SIMS 5, IONTOF, Germany). Microscopic analyses on nanostructures of as-synthesized $CsPbBr_3$ PQDs and $CsPbBr_3$ PQD/PDMS film were conducted using transmission electron microscope (TEM; JEM-F200, JEOL, Japan). $CsPbBr_3$ PQDs dispersed in *n*-hexane were placed on a carbon coated Cu-grid (01820, Ted Pella, USA) and dried in a desiccator overnight. $CsPbBr_3$ PQD/PDMS film was prepared in a thickness of approximately 100 nm using an ultramicrotome (MTX, RMC, USA).

2.6. Steady-state PL characterization

The absorption and PL emission spectra of the synthesized $CsPbBr_3$ PQDs and $CsPbBr_3$ PQD/PDMS films were collected at RT using an ultraviolet–visible (UV–Vis) spectrometer (Lambda 365, PerkinElmer, USA), and a fluorescence (FL) spectrophotometer (FL-7100, Hitachi High-Tech, Japan, respectively. An argon lamp with a 365 nm excitation wavelength was irradiated. The PL emission within the sample was collected with a photomultiplier tube (PMT) detector operated at 400 V at a scan rate of 240 nm/min. When the PL intensity exceeded the measurement limit (9999.9) of the FL spectrometer, a K&F variable neutral density filter was applied. The PLQY was examined by a fluorescence spectrometer equipped with an integrating sphere (FS-2, Scinco, Korea).

2.7. Time-resolved PL characterization

The time-resolved PL (TRPL) decay was obtained by a custom-built time-correlated single-photon counting (TCSPC) system. A mode-locked Ti:sapphire laser (MaiTai BB, Spectra-Physics, USA) with an ultrashort pulse FWHM of 80 fs at a central wavelength of 800 nm was utilized as an excitation light source. The intrinsic repetition rate of 800 MHz was reduced to 800 KMz by a custom-built pulse picker, and the frequency of pulse-picked output was doubled using a 1 mm-thick beta barium borate crystal (type I, $\theta = 29.2^\circ$, EKSMA Optics, Lithuania) to generate 400 nm excitation wavelength from 800 nm. The PL decays of the films were measured with multiple laser powers modulated by a neutral density filter. The PL emission of excited film was collected with microchannel plate photomultiplier (R3809U-51, Hamamatsu, Japan). The response function of the overall system has an FWHM of approximately 25 ps?

2.8. Cross-sectional PL mapping with confocal laser scanning microscope system

The sample was prepared by slicing film with a razor blade at a thickness under 500 μm just before analysis to minimize the exposure of the sliced sample to the external environment. Imaging was performed on a confocal laser scanning microscope system (CLSM; LSM 880, Carl Zeiss, Germany) at RT using a 405 nm laser with a 10 × objective. The FL of sample was collected with a detector in the range of 410 nm to 575 nm.

3. Results and discussions

3.1. Synthesis and optical analysis of AEP-treated $CsPbBr_3$ PQD/PDMS film

3.1.1. Synthesis of AEP-treated $CsPbBr_3$ PQD/PDMS film

The synthesis scheme of free-standing and flexible $CsPbBr_3$ PQD/PDMS film is depicted in Fig. 1a, wherein the comprehensive procedure is detailed in the 'Material and Methods'. Initially, $CsPbBr_3$ PQDs were prepared by employing conventional hot injection method, utilizing a ligand pair comprising OAm and OA. TEM analysis confirmed the average particle diameter of synthesized $CsPbBr_3$ PQDs to be 12.56 nm ± 2.95 nm (Fig. S1). The measured lattice interplanar spacing, 5.5 Å, matches the (100) crystallographic spacing of the cubic ɑ-phase $CsPbBr_3$. UV–Vis absorption and PL emission spectra of $CsPbBr_3$ PQDs dispersed in *n*-hexane are shown in Fig. S2. $CsPbBr_3$ PQDs exhibited a strong green emission at 516.8 nm upon the excitation with 365 nm UV light, corroborating previously reported results [31]. To augment the PL difference between pre- and post-AEP treatment for efficient optical encryption, the surface defects on $CsPbBr_3$ PQDs were further induced *via* additional ligand purification step. This process resulted in the removal of ammonium cation ligands occupying Cs site from the PQDs' surface, generating numerous surface vacancies at Cs site (V_{Cs}) (Fig. 1b) [27,32]. Fig. S3 shows the cross-sectional image of synthesized $CsPbBr_3$ PQD/PDMS film obtained by SEM. EDS mapping for cesium (Cs), lead (Pb), and bromide (Br) on an enlarged image of $CsPbBr_3$ PQDs embedded within the PDMS matrix (× 16 000) verified the inclusion of $CsPbBr_3$ PQDs in the PDMS matrix. Notably, the X-ray signal for Cs was barely detectable, implying that the predominant surface defects are V_{Cs} generated during the film's synthesis process. The film thickness was formed at around 200 μm, as validated by optical microscope (OM) image, covering the AEP treatment's penetration depth (Fig. S4).

3.1.2. Optical property of $CsPbBr_3$ PQD/PDMS film upon AEP treatment

The optical properties of $CsPbBr_3$ PQD/PDMS film were examined throughout the synthesis process including AEP treatment, supporting the effective passivation of V_{Cs} by diffusion of Ag^+ ions from AEP into the PDMS matrix as illustrated in Fig. 1b and c, with further confirmation provided at the following section 3.2. After AEP treatment, the color of $CsPbBr_3$ PQD/PDMS film transitioned into a brighter yellow (Fig. 1d) and displayed enhanced green emission under 365 nm UV light (Fig. 1e). To evaluate the optical properties throughout the synthesis process, UV–Vis absorption and PL emission spectra of $CsPbBr_3$ PQD/PDMS composite were measured at each synthesis step (Fig. 1f). As-synthesized $CsPbBr_3$ PQDs were spin-coated on a wafer measuring 5×10 mm^2 with the same amount (30 μL) across a comparable area of $CsPbBr_3$ PQD/PDMS film for analysis. The spin-coated $CsPbBr_3$ PQD film exhibited a peak at 507 nm in the absorption spectra and a peak at 520 nm in the PL spectra. When the purified $CsPbBr_3$ PQDs were mixed with PDMS prepolymer, the intensity of the emission peak significantly attenuated to less than half compared to that of the spin-coated $CsPbBr_3$ PQD film. A subsequent cross-linking process resulted further reduction in the PL intensity of the synthesized $CsPbBr_3$ PQD/PDMS film to 6.2 % of the spin-coated $CsPbBr_3$ PQD film, equating to a PLQY of 1.4 %. Notably, some of key factors known to degrade $CsPbBr_3$ PQDs upon cross-linking process are 1) the formation of surface vacancies following the desorption of ligand molecules [27,32] and 2) the aggregation of PQDs due to the discrepancy in polarity between PQDs and polymer during the film fabrication [33–36]. The aggregation of PQDs is corroborated by red-shift in the emission peak from 519 nm to 527 nm after the cross-linking process (Fig. 1f) [37–39]. AEP-treated $CsPbBr_3$ PQDs/PDMS film (henceforth denoted as AEP-treated film) demonstrated a green emission at 522 nm, with a significantly elevated PL intensity (9-fold enhancement compared to $CsPbBr_3$ PQD/PDMS film (denoted as pristine film)). Consequently, this improvement led to an elevation in PLQY from 1.4 % up to an average of 20 % (maximum 20.7 %).

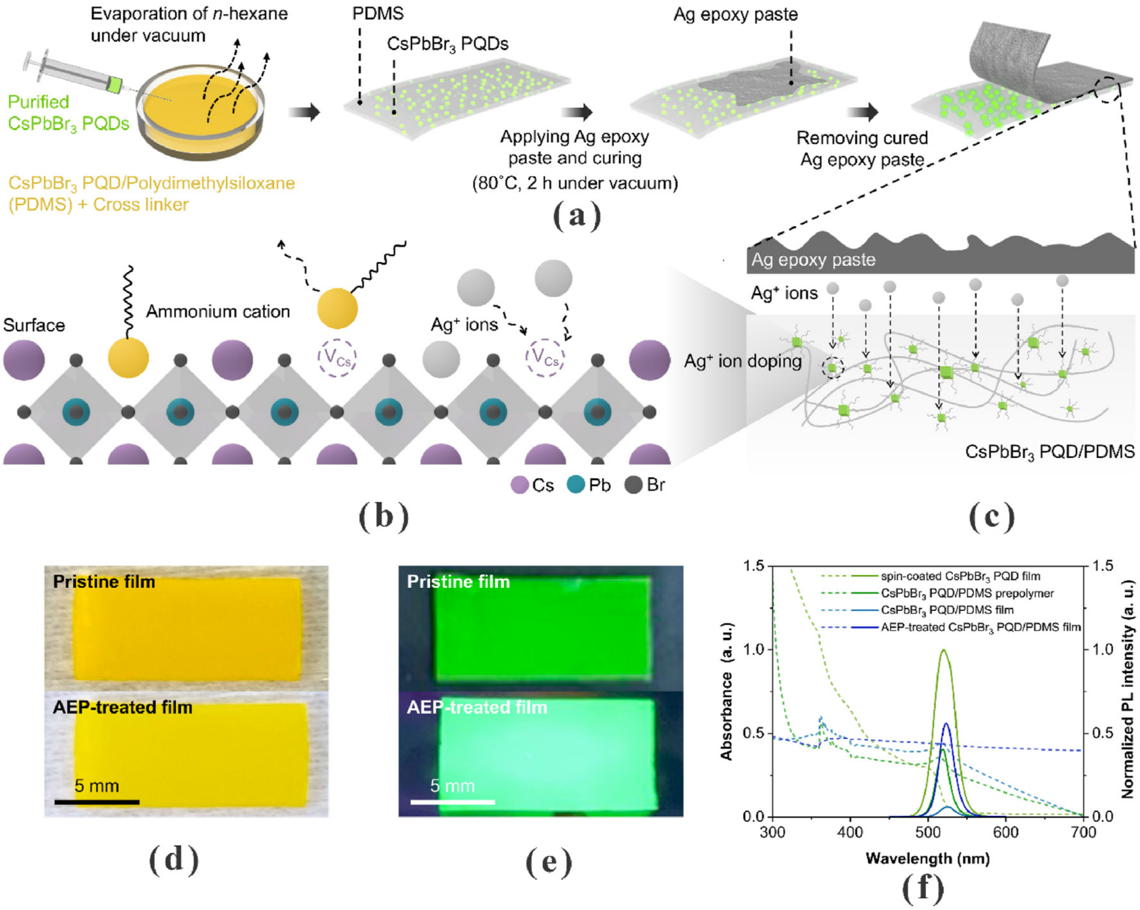

Fig. 1. Synthesis and optical analysis of AEP-treated $CsPbBr_3$ PQD/PDMS film. (a) Synthesis process of $CsPbBr_3$ PQD/PDMS film and AEP treatment process. (b) Schematic illustration of $CsPbBr_3$ PQD's surface with ligands, highlighting the defect passivation by Ag^+ ions from AEP treatment. (c) Schematic interface depiction between AEP and $CsPbBr_3$ PQD/PDMS film. Comparative optical photographs of $CsPbBr_3$ PQD/PDMS film before (top) and after (bottom) AEP treatment under (d) daylight and (e) UV light at 365 nm. (f) Comparative absorption (dashed line) and PL emission (solid line) spectra for spin-coated $CsPbBr_3$ PQD film, $CsPbBr_3$ PQD/PDMS prepolymer, $CsPbBr_3$ PQD/PDMS film, and AEP-treated $CsPbBr_3$ PQD/PDMS film (normalized to the peak emission intensity of the $CsPbBr_3$ PQD film).

3.2. *Characterization of the AEP-treated $CsPbBr_3$ PQD/PDMS film*

3.2.1. *Morphological and compositional characterization of AEP-treated film*

FT-IR spectroscopy was conducted to analyze the chemical structure changes in the PDMS polymer matrix subsequent to AEP treatment (Fig. 2a). The characteristic absorption peaks located at 796 cm^{-1}, 1 018 cm^{-1}, 1 074 cm^{-1}, 1 259 cm^{-1}, and 2 962 cm^{-1} can be assigned to CH_3 rocking in S-CH_3, Si-O-Si stretching, CH_3 deformation in Si-CH_3, and CH_3 rocking in S-CH_3 of PDMS, respectively [40,41]. Remarkably, the FT-IR spectrum of $CsPbBr_3$ PQD/PDMS film closely resembled that of the pure PDMS film even after AEP treatment without any shifts in the characteristic peaks (Fig. S5). This similarity substantiates negligible chemical interactions between AEP and PDMS polymer chain, confirming the preservation of the nanocomposite's chemical structure throughout the treatment [42].

The surface property of $CsPbBr_3$ PQD/PDMS film upon AEP treatment was further investigated using water contact angle measurements (Fig. 2b, top). In this method, a 10 μL water droplet was placed on the film's surface and the contact angles were averaged from 5 measurements across the different regions in the film. The pristine film exhibited a contact angle of 98.86° ± 0.68° attributable to the hydrophobic nature of PDMS matrix. Following AEP treatment, the contact angle exhibited a minimal change (97.42° ± 0.86°), indicating a negligible change in the hydrophobicity of the film's surface after the detachment of AEP. AFM imaging of the film's surface morphology also supported that AEP treatment did not induce significant morphological deformations (Fig. 2b, bottom). The RMS surface roughness (R_q) of the film before and after AEP treatment was measured to be 0.001 7 μm and 0.002 8 μm, respectively, demonstrating a negligible variation in the surface roughness.

3.2.2. *Ag^+ ion doping in $CsPbBr_3$ PQD/PDMS film via AEP treatment*

Further compositional analysis was performed to examine the surface defect passivation by Ag^+ ions through AEP treatment. However, the low concentration of $CsPbBr_3$ PQD within the PDMS matrix limited the analysis on a macro scale. Table S1 displays the elemental concentration of diffused Ag^+ ions within the AEP-treated film, as analyzed by XRF. The AEP-treated film contained a trace amount of Ag (0.000 5 %), whereas no Ag was detected in the pristine film. The result of TOF-SIMS analysis indicated the absence of Ag within a depth of 1 nm from the surface after removing AEP, supporting that the trace amount of Ag identified by XRF, with detection depth of tens of μm, is not the residual AEP on the surface (Fig. S6). Also, ICP-MS analysis showed that the concentration of Ag in the sample solution increased from 82.28 ng/mL to 2 291.98 ng/mL after AEP treatment, indicating the existence of diffused Ag^+ ions within the AEP-treated film (Fig. 2c).

The doping of diffused Ag^+ ions into $CsPbBr_3$ PQDs was further explored *via* XRD analysis. The crystal structures of $CsPbBr_3$ PQDs in both pristine and AEP-treated films were examined by XRD diffraction patterns (Fig. 2d). To clarify the characteristic peaks of $CsPbBr_3$ PQDs in the diffraction patterns, the XRD peak attributable to PDMS (11.8°) was

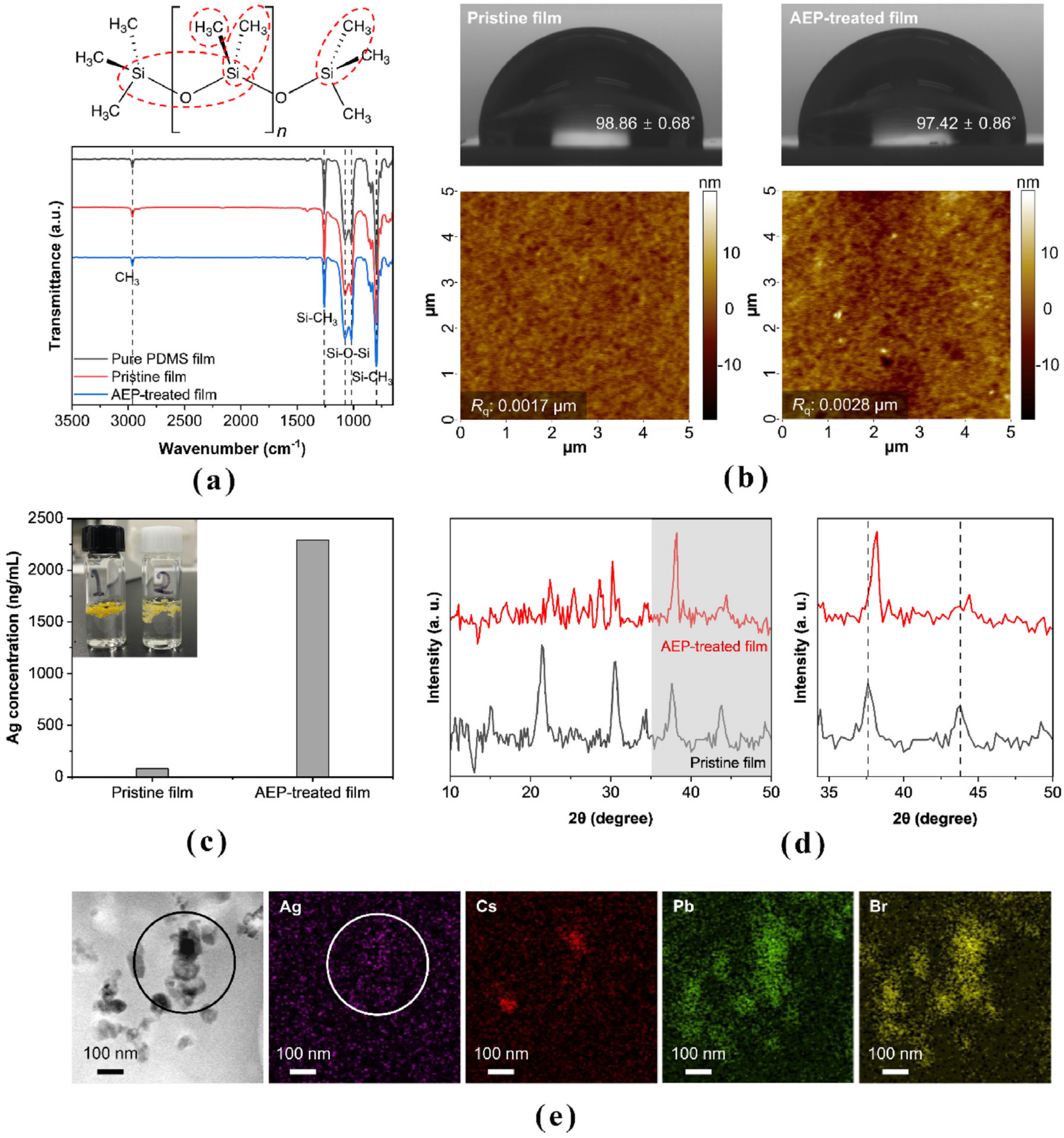

Fig. 2. Characterization of the AEP-treated $CsPbBr_3$ PQD/PDMS film. (a) Molecular structure of PDMS, with characteristic chemical groups highlighted by dashed red circles, alongside with FT-IR spectra comparison among pure PDMS, pristine, and AEP-treated films. (b) Water contact angles (top) and AFM images (bottom) for the pristine and AEP-treated films, including the root-mean-square (RMS) surface roughness (R_q). (c) ICP-MS analysis of $CsPbBr_3$ PQD/PDMS films before and after AEP treatment (inset: sliced $CsPbBr_3$ PQD/PDMS films soaked in Ag etchant solution (NH_4OH:H_2O_2:EtOH = 1:1:4 (mL)), 1 — pristine film, 2 — AEP-treated film). (d) XRD patterns of the pristine and AEP-treated films, focusing on the magnified XRD patterns to the right, highlighted in a gray colored box on the left spectrum. (e) TEM images of $CsPbBr_3$ PQDs within the AEP-treated film, accompanied by elemental mapping for Ag, Cs, Pb, and Br, where black and white circles highlight $CsPbBr_3$ PQDs-enriched and Ag-enriched regions, respectively.

subtracted from the original diffraction patterns of $CsPbBr_3$ PQD/PDMS film (Fig. S7). The existence of cubic $CsPbBr_3$ PQDs in the pristine film was characterized by observed peaks at 15°, 21.4°, 30.4°, 34.4°, 37.6°, 43.8°, and 49.2°, corresponding to the reflections from the (100), (110), (200), (210), (211), (220), and (310) planes, respectively. In addition, the incorporation of metal ions into perovskite crystals is typically revealed through alterations in the peaks of XRD, where the variations in XRD peaks exhibit distinct patterns contingent upon the ionic radius of the doped metal ion. In detail, when the ionic radius of the metal ion is larger than that of ions within the doping site, the characteristic XRD peaks are observed to shift towards higher angles with asymmetric peaks [28,43]. This alteration may be interpreted as a lattice shrinkage and lattice distortion (octahedral tilting) in the perovskite crystal. With an increase in doping concentration, the asymmetric peaks tend to divide into multiple peaks, eventually attenuated and indiscernible with excessive doping [43,44]. Conversely, in cases where the ionic radius of the doped metal ion matches or closely resembles that of the original ions at the doping site, little or no alteration in XRD pattern are apparent, indicating the absent of changes in crystal lattice [23,45,46]. As demonstrated in Fig. 2d, the characteristic peaks of $CsPbBr_3$, corresponding to (211) and (220) plane, exhibited a shift towards higher angles upon AEP treatment, with values changing from 37.6° to 38.2°, and from 43.8° to 44.4°, respectively [47]. Additionally, the reduction in the collective X-ray signal, coupled with an asymmetric shape, revealed the octahedral tilting in $CsPbBr_3$ PQDs as a result of Ag $^+$ ion doping (Fig. S7). Hence, it can be deduced that Ag^+ ions with an ionic radius of

1.26 Å are incorporated into the vacancies in the Cs site (V_{Cs}) with a larger ionic radius (1.81 Å), rather than the Pb site, which has a comparable ionic radius (1.19 Å) to the Ag^+ ions [28,44].

This claim can be augmented through the calculation of the Goldschmidt tolerance factor (t_G), which indicates the degree of lattice distortion in perovskite crystals. The Goldschmidt tolerance factor is calculated using Eq (1), in which R_A, R_B, and R_X represent the ionic radii of cations A, B, and anions X comprising the perovskite crystal (ABX_3). A tolerance factor ranging from 0.8 to 1 leads to the formation of an ordered cubic structure with limited distortion, while a tolerance factor below 0.8 triggers octahedral tilting, resulting in a distorted crystal structure with reduced symmetry. The calculated tolerance factor of pristine $CsPbBr_3$ PQD was 0.85, implying a stable lattice structure with limited distortion. If we assume Ag^+ ions completely replace Cs^+ ions in the Cs site, the tolerance factor becomes 0.72 indicating significant lattice distortion. In contrast, doping in the Pb site results in a tolerance factor of 0.83, maintaining a stable lattice structure. As a result, the lattice distortion in $CsPbBr_3$ PQDs, as observed in XRD patterns, aligns with the calculated tolerance factor exclusively when Ag^+ ions are introduced as dopants in V_{Cs}.

Although XPS was conducted to further confirm the Ag^+ ion doping in V_{Cs}, the electron signals corresponding to Cs, Pb, Br, and Ag were barely detectable due to the low concentration of $CsPbBr_3$ PQDs in the PDMS matrix, as mentioned above (Fig. S8). Therefore, alternative XPS analysis was conducted on a $CsPbBr_3$ PQD single layer film treated with modified AEP treatment using $CsPbBr_3$ PQD/PDMS bilayer structure. In detail, the bilayer PQD/PDMS film was prepared by sequentially spin-coating $CsPbBr_3$ PQDs and PDMS onto a silicon wafer, followed by curing in vacuum oven. Subsequently, AEP treatment was conducted on the top of PDMS layer. During this procedure, Ag^+ ions infiltrate PDMS layer and are doped in $CsPbBr_3$ PQD layer, as evidenced by the enhancement in PL intensity (Fig. S9). After AEP treatment, the PDMS layer was detached, leaving behind only Ag^+ ion doped $CsPbBr_3$ PQD single layer on the Si wafer. The XPS peaks of multiple elements including Cs, Pb, Br, C, and O were observed and calibrated using the C 1s peak (Fig. S10), while Ag was not detected either in the pristine or AEP-treated $CsPbBr_3$ PQD single layer film owing to its low concentration. Through XPS peak-differentiation-imitating analysis, the high-resolution spectra of Cs 3d, Pb 4f, and Br 3d were analyzed (Fig. S11). As shown in Fig. S11a, the Cs $3d_{3/2}$ and $3d_{5/2}$ peaks, located at 738.0 eV and 724.0 eV, respectively, showed negligible shifts after AEP treatment, implying no significant interaction between doped Ag and Cs. The Pb 4f spectrum displayed two distinct peaks corresponding to Pb^{2+} 4f, specifically Pb^{2+} $4f_{5/2}$ at 143.0 eV and Pb^{2+} $4f_{7/2}$ at 138.2 eV, alongside shoulder peaks indicative of metallic Pb^0 4f at 141.8 eV and 137.2 eV (Fig. S11b). Upon AEP treatment, all Pb 4f peaks exhibited a shift of approximately 0.2 eV towards lower binding energies, with a slight suppression of the Pb^0 peaks. The reduction in binding energy was also evident in the Br 3d spectrum, where the Br $3d_{3/2}$ and Br $3d_{5/2}$ peaks shifted from 69.4 eV to 69.1 eV and from 68.2 eV to 68.0 eV, respectively (Fig. S11c). In summary, the shifts to lower binding energies of Pb and Br – in contrast to the stable Cs peaks – suggest a decrease in the strength of Pb-Br interactions following AEP treatment [48], resulting in a decrease in the overlap of metal-halide orbital in perovskite crystal, predominantly triggered by octahedral tilting [43]. Accordingly, it is inferred that Ag^+ ions are doped in V_{Cs} of $CsPbBr_3$ PQDs embedded within PDMS matrix upon AEP treatment, inducing lattice distortion in $CsPbBr_3$ PQDs.

$$t_G = \frac{R_A + R_X}{\sqrt{2}(R_B + R_X)} \tag{1}$$

To further validate the diffusion and doping of Ag^+ ions into the $CsPbBr_3$ PQDs within the PDMS matrix, TEM images of the AEP-treated film were also obtained. Fig. 2e shows the cross-sectional TEM images of aggregated $CsPbBr_3$ PQDs (~100 nm) in the PDMS matrix and EDS mapping for compositional characterization. The elemental mapping of Ag confirms the presence of Ag^+ ion in the polymer matrix, with a content of 2.42 %. The Ag-enriched region in the EDS map (indicated by a white circle) was correlated with the aggregated $CsPbBr_3$ PQDs (demonstrated as a black circle in the TEM image), indicating the incorporation of Ag^+ ions into $CsPbBr_3$ PQDs.

3.3. *Photophysical properties of $CsPbBr_3$ PQD/PDMS film after AEP treatment upon various durations and temperatures*

AEP treatment durations (*t*) and temperatures (*T*) were examined to optimize AEP treatment process. Fig. 3a shows optical images of the AEP-treated films subjected to treatment at $T = 25$ °C (RT), 60 °C, 80 °C, and 100 °C with varied treatment durations ($t = 1$ h, 2 h, 4 h, 8 h, and 24 h). Along with the optical images, qualitatively measured PL intensities were presented as relative values, expressed as a ratio of AEP-treated film ($I_{treated}$) to pristine film ($I_{pristine}$) on average of 5 trials (Fig. 3b). Compared to the pristine film, the AEP-treated films exhibited a notable enhancement in PL intensity upon the treatment, an indicative of efficient passivation of surface defects on $CsPbBr_3$ PQDs through Ag^+ ion doping during AEP treatment [28,49]. Notably, maximum enhancements in PL intensity were realized more rapidly at elevated temperatures: 24 h for RT, 4 h for $T = 60$ °C, 2 h for $T = 80$ °C, and 1 h for $T = 100$ °C. This accelerated enhancement at higher temperatures might be attributed to the increased diffusion rate of Ag^+ ions into $CsPbBr_3$ PQD/PDMS film, facilitating the defect passivation in a reduced timeframe, which will be discussed further in the 'Diffusion analysis' section [30]. The film subjected to AEP treatment at 80 °C for 2 h exhibited the highest PL intensity enhancement ratio of 8.75 ± 0.49, achieving a maximum PLQY of 20.7 %.

Meanwhile, the effect of thermal degradation of $CsPbBr_3$ PQDs became noticeable under prolonged treatment durations at temperatures exceeding RT [50]. At $T = 60$ °C, the PL intensity enhancement persisted up to 4 h of treatment (6.85 ± 0.54), beyond which saturation occurred at extended treatment durations. At higher temperature ($T = 80$ °C and 100 °C), the effect of thermal degradation became more apparent, leading to a subsequent decline and eventual saturation of the films' PL intensity. This reduction in PL intensity intensified and accelerated with increasing treatment temperature. After 24 h of treatment, the relative PL intensities decreased from 8.75 ± 0.49 to 6.57 ± 1.53 (24.92 %) at $T = 80$ °C, and from 5.52 ± 0.28 to 4.37 ± 0.42 (20.83 %) at $T = 100$ °C. To note, the film treated at $T = 100$ °C exhibited the low enhancement ratio of 5.52 after 1 h of AEP treatment compared to those of $T = 80$ °C and 60 °C, implying that the thermal degradation of PQDs becomes significant at higher temperature.

The interplay between thermal degradation and defect passivation was further evidenced by an auxiliary experiment (Fig. S12). Specifically, two films were subjected to the heat treatment at 100 °C for 8 h, with AEP removed after 1 h for one film (dash-dot line) and retained for another film (solid line). In the absence of continued defect passivation, the former exhibited a more pronounced decrement in the PL intensity, attributable to the enhanced thermal degradation of $CsPbBr_3$ PQDs.

In the AEP-treated films, blue shifts in the PL peak from 527 nm to (521~523) nm were observed within 1 h of AEP treatment, regardless of treatment temperatures (Fig. 3c). The shifts in PL emission peaks are ascribable to the surface defect passivation by Ag^+ ions in V_{Cs}. As abovementioned, the discrepancy in ion radii between Cs^+ (1.81 Å) and Ag^+ (1.26 Å) provokes an octahedral tilting in the crystal lattice of $CsPbBr_3$ PQDs, leading to the reduction in the degree of Pb-Br orbital overlap. Since the bandgap energy of perovskite is inversely proportional to the strength of metal-halide orbital overlap, approximately 0.03 eV increase in the bandgap energy of $CsPbBr_3$ PQD was observed, resulting in a blue-shifted emission of AEP-treated films [51]. This is consistent with the peak attenuation observed in the XRD and XPS analysis, stemming from the octahedral tilting in $CsPbBr_3$ PQDs upon AEP treatment.

Surface defect passivation *via* AEP treatment was further analyzed by examining the exciton dynamics in the AEP-treated film (80 °C, 2 h)

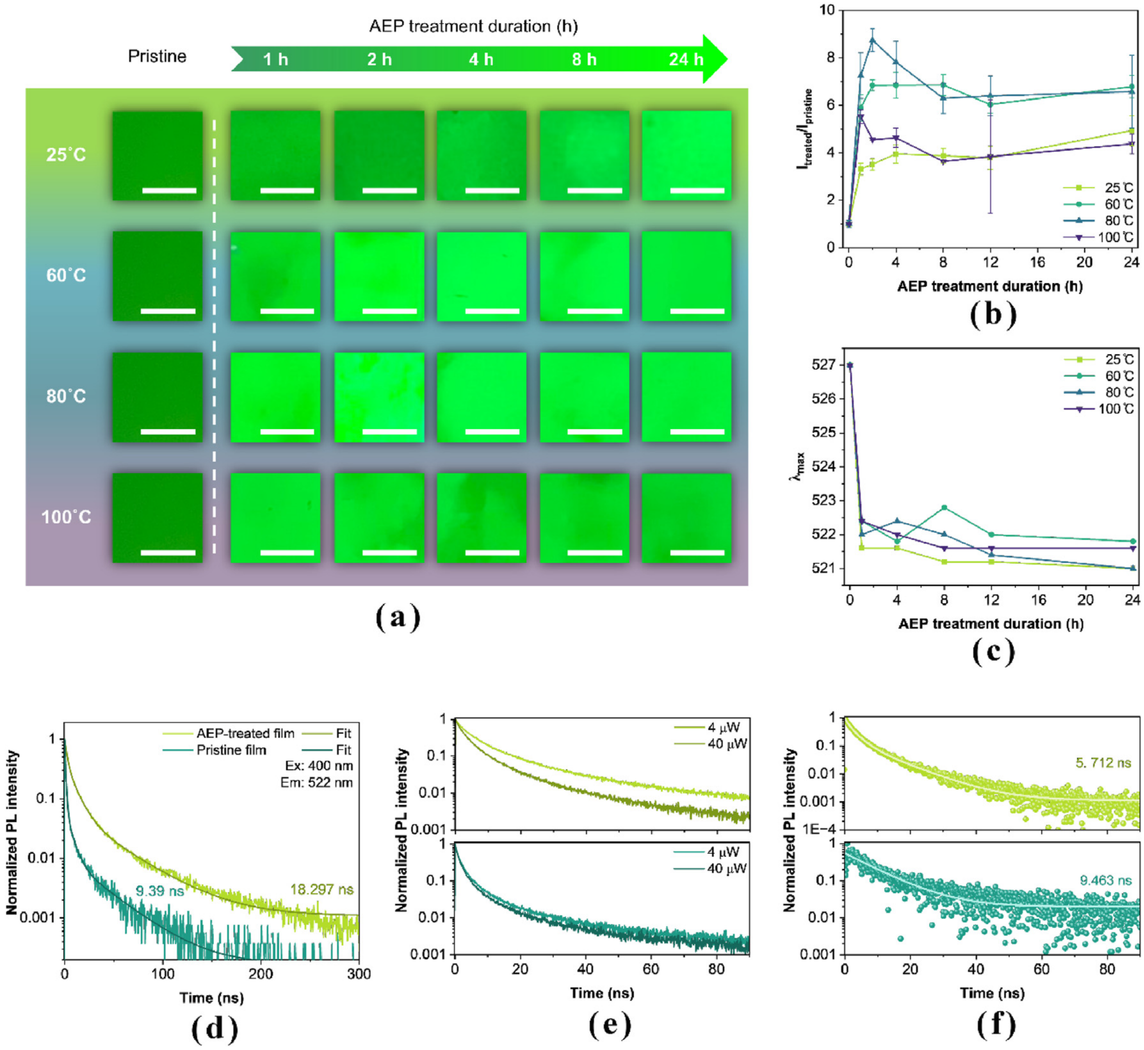

Fig. 3. Variations in the photophysical behavior of $CsPbBr_3$ PQD/PDMS film following AEP treatment across different treatment durations and temperatures. (a) Optical images of the AEP-treated film under UV light at various treatment durations and temperatures (scale bar of 2.5 mm). (b) Changes in relative PL intensity and (c) shifts in the PL emission peak for the AEP-treated film under various treatment durations ($t = 1$ h, 2 h, 4 h, 8 h, and 24 h) and temperatures ($T = 25$ °C (RT), 60 °C, 80 °C, and 100 °C). (d) Comparative TRPL decay profiles for the pristine film and AEP-treated film. (e) Pump-fluence dependent PL decay dynamics and (f) subtracted biexciton component decay of the AEP-treated film (top) and pristine film (bottom).

through TRPL measurements (Fig. 3d). The PL decay profiles of both pristine and AEP-treated films were modeled using a tri-exponential function, with specific component values detailed in Table S2. Post-AEP treatment, the PL decay detained compared to the pristine film, with an average PL lifetime (τ_{avg}) increased from 9.39 ns to 18.297 ns? Notably, this observation underscores that AEP treatment effectively diminished defect sites, thereby reducing the probability of non-radiative recombination and elongating exciton lifetime.

To further elucidate the multi-exciton recombination dynamics following AEP treatment, exciton dynamics under varying excitation fluences were measured within a shorter time window of 100 ns? Generally, Auger recombination process is governed by the annihilation of excitons *via* exciton-exciton Coulomb interactions. Consequently, the probability of biexciton Auger recombination heightens with an increase in the initial exciton density and excitation fluence, leading to a reduced exciton lifetime [52]. These measurements employed 4 μW and 40 μW to establish low and high excitation fluence conditions, respectively (Fig. 3e). The low excitation fluence was determined when the detector could barely discern the PL signal from the pristine film. As the excitation fluence intensified, the PL decay of AEP-treated film accelerated, attributed to a higher probability of biexciton Auger recombination due to enhanced exciton densities. In contrast, the PL decay rate of the pristine film remained consistent across varying excitation fluence, indicating that exciton recombination within the pristine film was initially dominated by non-radiative Auger recombination. The biexciton decay components were obtained by subtracting the tail-normalized low fluence decay from high fluence decay (Fig. 3f) [53]. The mean biexciton lifetime in the AEP-treated film was determined to be 5.712 ns, notably shorter than that of the pristine film (9.463 ns). This discrepancy might be attributed to an accelerated exciton annihilation mediated by Auger recombination, resulting from higher initial charge carrier densities. The AEP-treated film exhibited a higher initial charge carrier density compared to the pristine film under equivalent photon fluence, demonstrating an enhancement in the PLQY of $CsPbBr_3$ PQDs embedded within the PDMS matrix upon AEP treatment.

3.4. Analysis of Ag^+ ion diffusion and PL intensity dynamics of AEP-treated film

3.4.1. Analysis of Ag^+ ion diffusion upon AEP treatment via CLSM

The CLSM imaging system is widely utilized for measuring non-steady state molecular diffusion dynamics of fluorescent molecules (*e.g.*, fluorescently labeled proteins, fluorescent dyes) within various substances [54–56]. In our study, CLSM was employed to elucidate the diffusion dynamics underlying AEP treatment. The mechanism of defect passivation through AEP treatment involves the diffusion of Ag^{+} ions into the PDMS matrix and their subsequent doping onto the surface of PQDs. Assuming a uniform doping of Ag^{+} ions and no thermal degradation of PQDs, the PL intensity can be depicted as a linear function of Ag^{+} ion concentration. Under this assumption, a diffusion model was formulated by modifying the analytic solution to Fick's second law, drawing on insights from the prior studies on diffusion in PDMS [54,55]. Based on Fick's second law in semi-infinite medium, the PL intensity at depth *x* from the surface after AEP treatment for a duration *t* is given by:

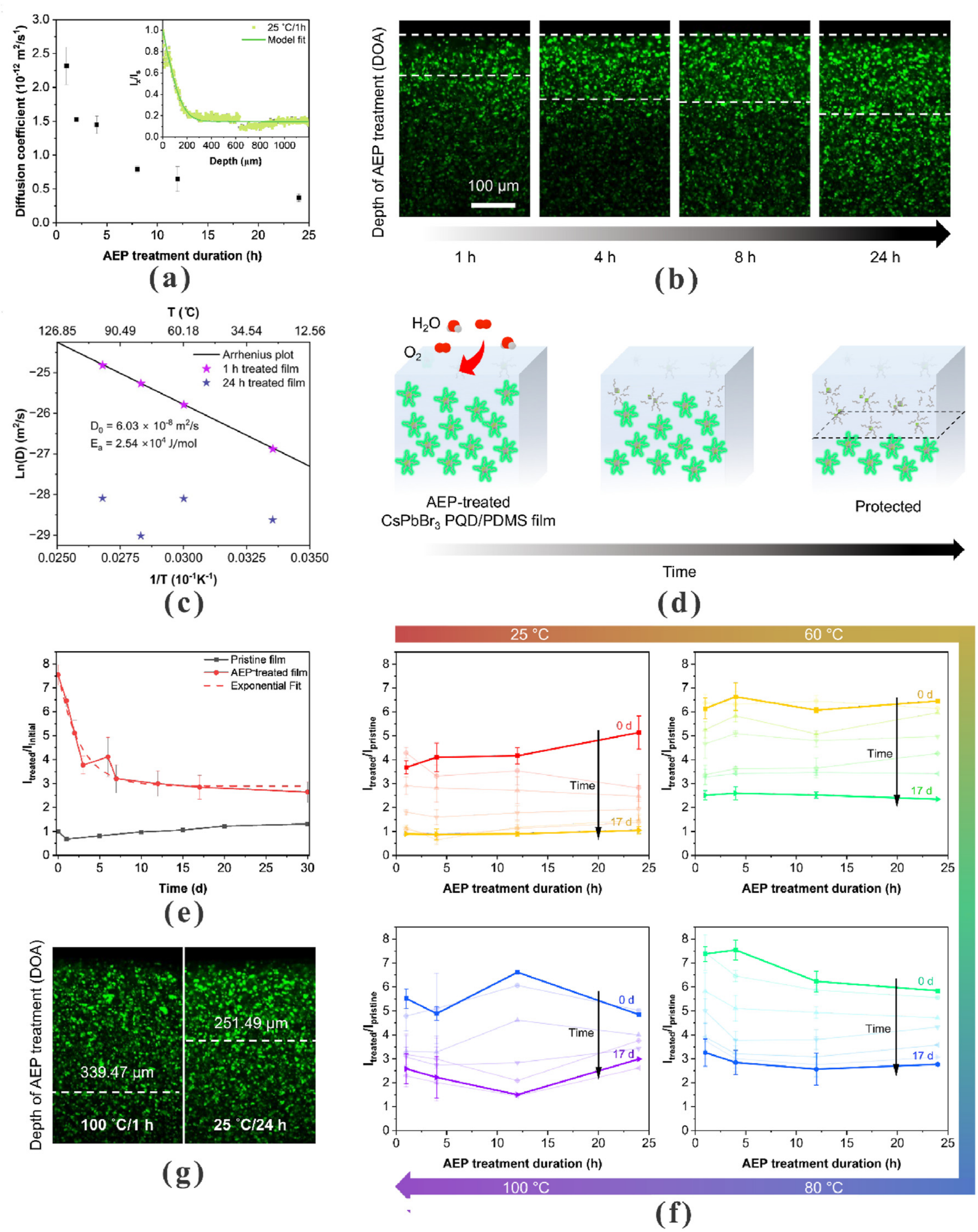

Fig. 4. Analysis of Ag^{+} ion diffusion and PL intensity dynamics of AEP-treated film. (a) Time dependency of diffusion coefficients for films treated at $T = 25$ °C, alongside the PL intensity profiles for films treated for 1 h at $T = 25$ °C (inset), fitted according to Eq (2). (b) CLSM images of films treated at $T = 25$ °C, illustrating variations in treatment duration (depth of AEP treatment (DOA) is denoted by the gap between the white dashed lines). (c) Measured diffusion coefficients across various treatment temperatures for a consistent AEP treatment duration of 1 h (purple) and 24 h (blue) with Arrhenius plot displaying the infinite diffusion coefficient and the activation energy of films treated for 1 h. (d) Schematic degradation process of the AEP-treated film. (e) Long-term PL intensity dynamics of the pristine and AEP-treated films in ambient condition. (f) AEP treatment temperature- and duration-dependent long-term PL intensity dynamics organized in a clockwise manner. (g) CLSM images of films treated at $T = 100$ °C for 1 h (left) and $T = 25$ °C for 24 h (right) with DOAs.

$$\frac{I(x,t)-I_0}{I_s-I_0}=1-\mathrm{erf}\left(\frac{x}{2\sqrt{Dt}}\right) \tag{2}$$

where I_0 and I_s denote the infinite background intensity and surface intensity, respectively; D denotes the diffusion coefficient, and erf represents the error function. I_0 was experimentally determined to be the average PL intensity value at which the gradient $\delta I_x/\delta x$ is less than 10^{-4}. I_s was identified as the maximal intensity value proximal to the AEP-treated film surface. The depth of AEP treatment (DOA) was determined as $(Dt)^{1/2}$, the equation for calculating the diffusion length. Utilizing MATLAB software, the PL intensity profile across the entire field of view was computed. Intensity values along each line parallel to the film surface were averaged and normalized against I_s to mitigate errors stemming from non-continuous PL signals. Ensuring the semi-infinite nature of the medium, the analysis was performed on the films exceeding 1 mm in thickness, substantially surpassing the characteristic diffusion depth.

Since diffusion kinetic of AEP treatment is most dominant at $T = 25$ °C (thermal degradation becomes significant as temperature increases), experimentally measured PL intensity profiles of films treated at $T = 25$ °C were fitted to the modified solution in Eq (2) for various treatment durations ($t = 1$ h, 2 h, 4 h, 8 h, 12 h, and 24 h) utilizing least-squares approximation with variation in the diffusion coefficient D (Fig. 4a). The inferred values of diffusion coefficient and DOA are presented in Table S3. An increase in treatment duration from 1 h to 24 h corresponded with a decrease in the diffusion coefficient from $2.32 \pm 0.28 \times 10^{-12}$ m^2/s to $3.69 \pm 0.58 \times 10^{-13}$ m^2/s. Concurrently, DOA exhibited a rise from 91.20 ± 5.44 μm to 178.16 ± 14.04 μm, showing a linear dependency to $t^{1/2}$, which is generally accepted (Fig. 4b) [57]. The empirically derived D values were validated through temperature dependence analysis of the diffusion coefficient, employing the Arrhenius equation in Eq (3), where R denotes the molar gas constant, D_0 and E_a are the infinite diffusion coefficient and the activation energy, respectively. Following 1 h of AEP treatments at $T = 25$ °C, 60 °C, 80 °C, and 100 °C, diffusion coefficients were measured (Table S3). Then, D_0 and E_a were calculated by substituting six pairs of derived $\{(T_1, D_1), (T_2, D_2)\}$ in Eq (4) and averaged. The plotted Arrhenius relationship for Ag $^+$ ion diffusion in PDMS with averaged D_0 and E_a exhibited consistency with the experimentally measured diffusion coefficients, substantiating the diffusion analysis of the films treated for 1 h *via* CLSM (Fig. 4c).

$$D = D_0{}^{*}e^{-\frac{E_a}{RT}} \tag{3}$$

$$\frac{R^{*}\ln\frac{D_1}{D_2}}{\frac{1}{T_2}-\frac{1}{T_1}} = E_a \tag{4}$$

In contrast, with the prolongation of AEP treatment duration to 24 h, the experimentally measured diffusion coefficients exhibited a weak correlation with treatment temperature and could not be effectively explained by Arrhenius equation. This might be attributed to the limited efficacy of Ag$^+$ ion doping upon the prolongation of treatment duration at a higher temperature due to the thermal degradation of PQDs. This observation implies that the fluorescence-based diffusion analysis might not comprehensively depict the actual diffusion behavior of Ag$^+$ ions when the effect of thermal degradation exerts a significant influence.

The long-term PL dynamics of the AEP-treated films were examined using CLSM. As widely known, halide perovskite is vulnerable to long-term exposure to water and oxygen, resulting in the decomposition and dissolution of the perovskite crystal. In detail, the formation energy of halide defects decreases upon accumulation of water molecules, leading to the decomposition of the crystal [58]. Additionally, oxygen molecule generates a reactive superoxide O^{2-} which can react with the acidic A site cation under light irradiation, resulting in the decomposition of crystal [59]. In both processes, it is crucial to control the density of defects at which water or oxygen molecules can adsorb and initiate degradation process. Generally, the stability of PQDs towards water and oxygen is enhanced when PQDs are isolated from the external environment by encapsulation within a polymer matrix. Nevertheless, upon exposure to ambient conditions over several days, the AEP-treated film exhibited a region of quenched PL near the surface by interacting with diffused oxygen and water molecules within the PDMS matrix (Fig. S13). The structural instability of Ag $^+$ ion doped $CsPbBr_3$ PQDs in PDMS matrix, resulting from lattice shrinkage and distortion, results in accelerated degradation of PQDs upon exposure to oxygen and water molecules diffusing in the PDMS matrix.

In addition, as abovementioned, the calculated Goldschmidt tolerance factor (t_G) of Ag $^+$ ion doped $CsPbBr_3$ PQDs is 0.72, which is close to the range of significant lattice distortion in perovskite crystal ($t_G \leq 0.7$). This substantial lattice distortion results in the reductions in both ionic migration energy and halide defect formation energy, increasing the susceptibility of Ag $^+$ ion doped $CsPbBr_3$ PQDs to halide defects [60]. As a result, the inclusion of Ag $^+$ ions in $CsPbBr_3$ PQDs leads to accelerated degradation even with the trace amount of diffused water and oxygen, since the defects act as a channel for water and oxygen molecules to adsorb and initiate degradation process within the perovskite crystal [58,59,61]. This interaction caused an expansion of the quenched PL region from the surface (Fig. 4d) [62].

Furthermore, the PL intensities of AEP-treated film were monitored for 30 d after AEP treatment (Fig. 4e). Initially, the AEP-treated films exhibited a relative PL intensity of 7.5 ± 0.43 for the first 1 d to 2 d; however, a rapid quenching to 3.26 ± 0.57 was observed after 17 d. After 17 d, the quenching of PL intensity exponentially diminished and eventually saturated, likely due to the protection of Ag$^+$ ion-doped PQDs with PDMS matrix beneath the diffusion depth of water and oxygen molecules. Hence, PL intensity is expected to saturate at higher intensity with an increment of DOA. Conversely, the pristine film maintained its initial PL intensity for 30 d under ambient conditions, attributed to the protective role of the PDMS matrix in shielding structurally stable PQDs ($t_G = 0.85$) from environmental factors.

3.4.2. Time- and temperature-dependent long-term PL intensity of AEP-treated film

The long-term PL intensity dynamics of the AEP-treated films with various treatment conditions were monitored over a period of 30 days. The long-term dynamics of PL intensities in the AEP-treated films were presented until 17 d in Fig. 4f, as they exhibited minimal changes in PL intensities and saturated thereafter on average.

As demonstrated in Figs. 3b and 4f, the AEP-treated films exhibited dependency in their PL intensity with treatment duration immediately after the treatment (0 d) at fixed treatment temperature. In detail, a proportional relationship was observed at $T = 25$ °C, whereas an inverse proportional relationship was evident at $T = 80$ °C and 100 °C. Notably, all films exhibited a consistent quenching and saturation to similar intensity levels after 17 d despite the initial discrepancies in the PL intensities; films treated at $T = 25$ °C reached a saturated PL intensity of 0.9 ± 0.1, while those of films treated at $T = 60$ °C, 80 °C, and 100 °C achieved intensity level of 2.5 ± 0.1, 2.8 ± 0.3, and 2.3 ± 0.6 on average, respectively.

These observations suggest that the saturation level of quenched PL intensity is primarily determined by treatment temperature rather than duration. Particularly, the films treated at $T = 25$ °C for 24 h and $T = 100$ °C for 1 h displayed initial PL intensities of 5.1 ± 0.7 and 4.8 ± 0.1, respectively. Despite their similar initial PL intensities, the film treated at $T = 100$ °C for 1 h exhibited a higher saturated PL intensity of 3 ± 0.1 compared to the film treated at $T = 25$ °C for 24 h (1 ± 0.1), which exhibited DOAs of 339.5 μm and 251.5 μm, respectively (Fig. 4g). These results align with our assumption that saturated PL intensity enhances as DOA increases, which is also supported by the Arrhenius equation (Eq (3)) demonstrating the exponential relationship between diffusion coefficient and temperature.

3.5. Optical encryption and decryption strategies

Utilizing this unique PL intensity dynamics of the AEP-treated films with different treatment conditions, AEP treatment on $CsPbBr_3$ PQD/PDMS films emerges as a powerful encryption/decryption method (Fig. 5a). Initially, simple optical encryption was performed by patterning $CsPbBr_3$ PQD/PDMS film with AEP treatment, where decryption is facilitated under 365 nm UV light. Furthermore, by adjusting the conditions of the AEP treatment, a more sophisticated and secure form of time-dependent optical encryption can be realized.

The patterns were applied using stamps featuring various designs (Fig. S14). In the simple optical encryption patterning process, a 'Y' symbol was precisely imprinted onto the film using AEP, followed by a thermal treatment for 1 h at $T = 100$ °C. For the advanced time-dependent optical encryption, the surrounding region of the 'Y' symbol was coated with AEP and treated for an additional 24 h at $T = 25$ °C. After the patterning process, the AEP was removed. The basis for the temporal modulation of encryption and decryption lies in the difference of long-term PL intensity quenching rates, a consequence of varying treatment conditions, as depicted in Fig. 5b. Both sets of films treated at $T = 100$ °C for 1 h and at $T = 25$ °C for 24 h exhibited comparable PL intensities initially, rendering them indistinguishable by visual observation. However, the discrepancy in intensities between 100 °C/1 h-treated film and 25 °C/24 h-treated film increased significantly within 2 d, persisting for more than 15 d.

Optical images illustrating the decryption process of simple and time-dependent optical encryption/decryption are presented in Fig. 5c. Specifically, the 'Y' symbol from the simple optical encryption method remained invisible under daylight condition but was revealed with green fluorescence upon irradiation of 365 nm UV light. For the time-dependent optical encryption strategy, the encrypted pattern remained concealed under daylight and UV light irradiation for the initial hours

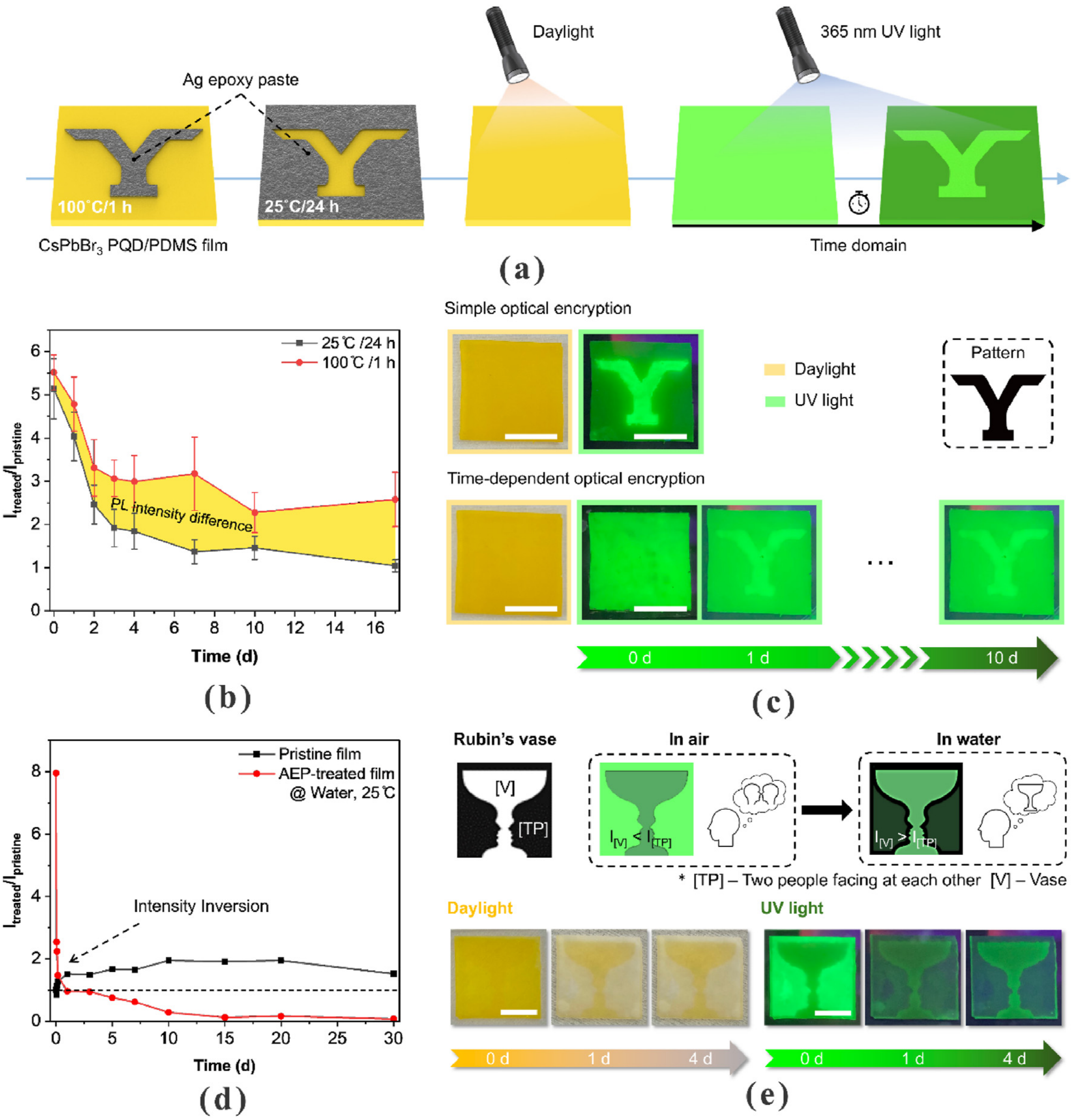

Fig. 5. Optical encryption and decryption strategies. (a) Schematic illustration of time-dependent optical encryption/decryption processes *via* AEP treatment. (b) Long-term PL intensities of 25 °C/24 h-treated film (black line) and 100 °C/1 h-treated film (red line) under ambient condition with yellow subtracted areas of the PL intensities. (c) Optical images of the 'Y' symbol obtained by both simple and time-dependent optical encryption/decryption processes under daylight and UV light (scale bar of 1 cm). (d) Long-term PL intensities of the pristine and AEP-treated films in water. (e) Schematic illustration of intensity inversion *via* Rubin's vase (top) and the optical images of water induced intensity inversion processes under daylight and UV light (bottom; scale bar of 1 cm).

following the treatment. As the PL intensity quenching accelerated in the 25 °C/24 h-treated background compared to the 100 °C/1 h-treated 'Y' symbol region, the emission in the 'Y' symbol became relatively stronger, being apparent under UV light after 1 d. The 'Y' symbol was observed after 10 d.

Furthermore, the AEP-treated film exhibited a significantly rapid quenching in PL intensity upon immersion in water (Fig. 5d). This phenomenon may be attributed to the attenuation in defect formation energy of $CsPbBr_3$ PQDs after AEP treatment as mentioned above, being more susceptible to the decomposition in aqueous environments. In contrast, the pristine film exhibited heightened stability in water over 30 d, alongside a slight increase in PL intensity. Although PQDs are inherently susceptible to water, their encapsulation within a polymer matrix offers protection and further passivation through the infiltration of water into the polymer matrix. Specifically, the entangled polymer chains facilitate the infiltration of a trace amount of water, which acts to passivate the surface defects in $CsPbBr_3$ PQDs by dissociating water into H_3O^+ and OH^- ions [5,63]. Consequently, the PL intensity of the pristine film increased while that of the AEP-treated film diminished upon immersion in water. During this process, an intensity inversion occurred as the PL intensity of the pristine film surpassed that of the AEP-treated film within a day.

Hence, the encrypted pattern demonstrated an intensity inversion reliant on environmental conditions (*e.g.*, air and water). This intensity inversion is effectively demonstrated by patterning a reversible figure, which induces ambiguity by exploiting multiple interpretations among multiple image forms (Fig. 5e). A classic example of such a reversible figure is 'Rubin's vase', interpretable either as a vase ([V]) or two people facing at each other ([TP]), contingent upon the observer's perspective. The [TP] region of 'Rubin's vase' was imprinted by AEP treatment, where the figure was initially perceived as [TP] due to the brighter green fluorescence under UV light. The intensity inversion occurred when the patterned film was immersed in water, with the figure transitioning to being recognized as [V] instead due to a reduction in the PL intensity of the [TP] region. Notably, the yellowish [TP] region gradually whitened, fully transitioning to white after 4 d under daylight, implying the decomposition of $CsPbBr_3$ PQDs within the [TP] region. Correspondingly, the green emission of the [TP] region diminished over time, whereas a slight increase in PL intensity was observed in the [V] region, attributable to the water-induced defect passivation. Accordingly, a distinct vase image emerged under both daylight and UV light within 4 d after immersion in water.

3.6. *Time-/environment-dependent optical encryption and decryption of $CsPbBr_3$ PQD/PDMS film*

Integrating the time-dependent optical encryption with the intensity inversion through water immersion, a multilevel advanced optical encryption was performed using AEP treatment on $CsPbBr_3$ PQD/PDMS film. As depicted in Fig. 6a, an array comprising four digits was fabricated by sculpting $CsPbBr_3$ PQD/PDMS film into the configuration of '8888'. These four independent digits were subsequently segmented into seven sections, each sequentially numbered in a counterclockwise orientation. Subsequent patterning with AEP was executed on each segment of digits corresponding to the pattern '0819', varying treatment conditions among the segments. In detail, the segments common to both '0819' and '1014' underwent treatment at $T = 100$ °C for 1 h, while the remaining segments were treated at $T = 25$ °C for 24 h. For instance,

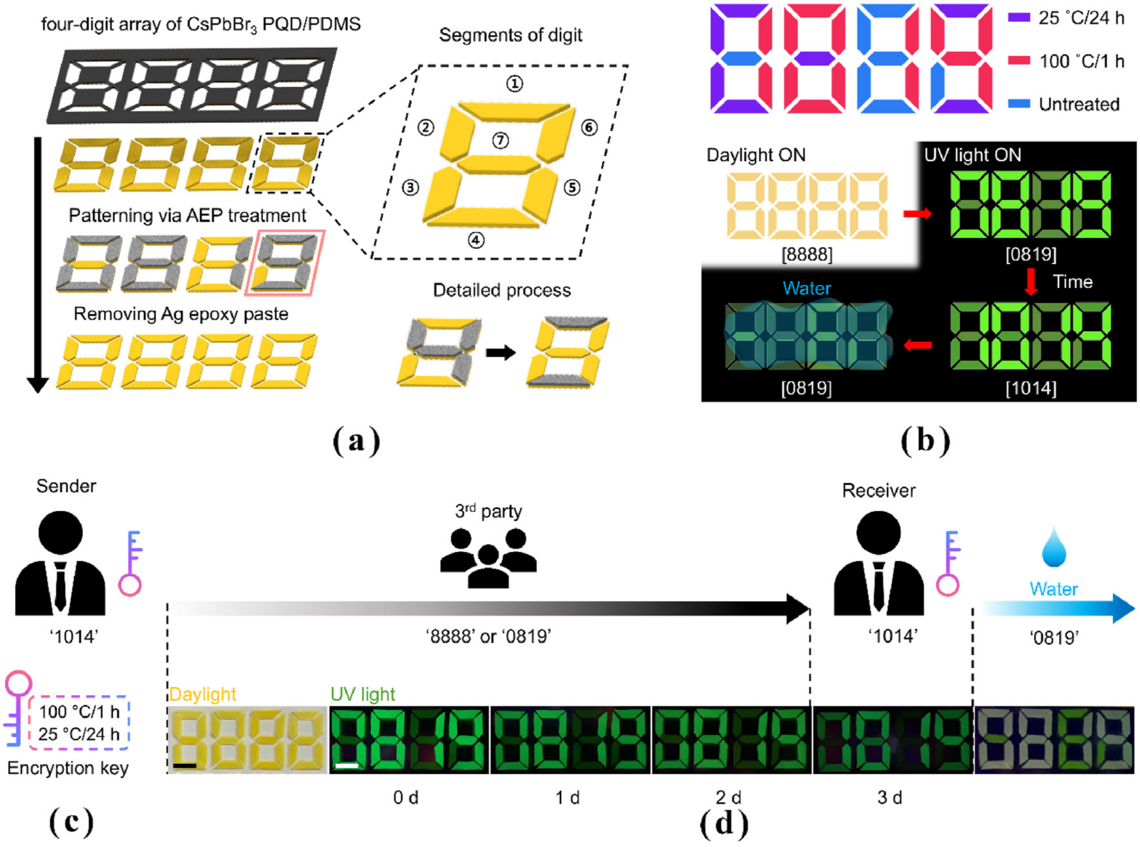

Fig. 6. Time-/environment-dependent optical encryption and decryption on $CsPbBr_3$ PQD/PDMS film. (a) Schematic illustration of the patterning process for a four-digit array on $CsPbBr_3$ PQD/PDMS film using AEP treatment, highlighting seven segments in a digit, numbered in a counterclockwise manner. (b) Original pattern design marked with different colors depending on the treatment conditions, alongside the pattern's decryption sequence. (c) Diagram of encryption/decryption process where a sender encrypts the message '1014' within '0819' and (d) sequential optical images displaying the evolution of the four-digit array over time (scale bar of 0.5 cm).

converting the digit '9' into '4' involved AEP treatment on segments 2, 5, 6, and 4 at $T = 100\,^{\circ}C$ for 1 h, whereas segments 1 and 4 were treated at $T = 25\,^{\circ}C$ for 24 h. Consequently, the red-colored regions were treated at $T = 100\,^{\circ}C$ for 1 h, and the purple-colored regions were treated at $T = 25\,^{\circ}C$ for 24 h, with no treatment conducted on the blue-colored regions (Fig. 6b).

Following the removal of AEP, the array under daylight visually represented the sequence '8888'. Upon exposure to UV light (365 nm), the array initially showed the sequence '0819' and gradually decrypted into '1014' under ambient air due to variations in the PL intensity quenching rates. The fully decrypted array was then immersed in water, permanently reverting to '0819' through intensity inversion between the treated and untreated regions, as schematically illustrated in Fig. 6b.

In a practical message transmission, a sender embedded the message '1014' within a decoy message '0819' on the digit array (Fig. 6c). By modulating AEP treatment conditions, the timeframe requisite for complete decryption became adjustable, thus serving as an encryption key. This encryption key was delineated as a pair of two distinct treatment conditions employed during the encryption process. In the presented case, the shared encryption key between the sender and receiver was defined as {(100 °C/1 h), (25 °C/24 h)}, indicating the utilization of AEP treatment at $T = 100\,^{\circ}C$ for 1 h and at $T = 25\,^{\circ}C$ for 24 h, with the corresponding decryption timeframe of 3 d. As demonstrated in Fig. 6d, while the message was in transit to the intended receiver (for 2 d following the encryption), the encrypted information within the array was safeguarded from third-party discovery, disguised with the fake information '8888' and '0819' under daylight and UV light, respectively. After 3 d, the intended receiver with the encryption key confirmed the decrypted message '1014' and subsequently immersed the array in water to obviate any post-transmission leakage of the decrypted information.

Our optical encryption strategy is compared with previous techniques using perovskite composite materials listed in Table S4, classified in several categories. While other optical encryption techniques involve complex processes (*e.g.*, 3D printing, hydrothermal or micro emulsion for material synthesis, multi-power laser engraving, and halide ion concentration control), our method using AEP treatment on $CsPbBr_3$ PQD/PDMS nanocomposite film has advantages of simple material preparation step and encryption procedure offering a multilevel encryption system. Furthermore, the decryption process necessitating only water and UV light bolsters user simplicity and security, and the cost associated with synthesis and patterning 1 cm^2 of $CsPbBr_3$ PQD/PDMS film using AEP was about 6.1×10^{-2} USD (Table S5). We also believe our optical encryption method could be augmented by employing Pb-free perovskite (*e.g.*, $CsSbBr_3$, $CsGeBr_3$) for environmental compatibility or by controlling the encryption/decryption operation time for desired application through regulation of environmental conditions such as humidity and temperature. Ultimately, the AEP treatment-based encryption technique presented in this work has the potential to further enrich the diversity of perovskite/polymer nanocomposites within advanced optical encryption frameworks.

4. Conclusions

In summary, a high-security multilevel optical encryption strategy attributed from the PL intensity enhancement *via* AEP treatment on $CsPbBr_3$ PQD/PDMS film was proposed. The introduction of Ag^+ ions by thermal treatment upon the application of AEP on the film effectively passivated surface vacancy defects within $CsPbBr_3$ PQDs, diminishing non-radiative exciton recombination. The AEP-treated film exhibited significantly enhanced PL properties, as evidenced through both steady-state PL and TRPL analyses, resulting in a 15-fold enhancement in PLQY (20.7 %) compared to the pristine film (1.4 %). Furthermore, CLSM analysis into the diffusion dynamics of Ag^+ ions furnished an in-depth insight into AEP treatment mechanism and long-term PL dynamics of the AEP-treated film. By harnessing the long-term PL dynamics *via* strategic AEP treatment condition adjustments, our methodology was employed as a time-dependent encryption method with disparities in the PL intensity quenching rates. Additionally, introducing a trace amount of water into $CsPbBr_3$ PQD/PDMS film patterned with AEP treatment facilitated an inversion in the PL intensities between the treated and untreated regions of the film. Integrating two strategies, a multilevel optical encryption was demonstrated on $CsPbBr_3$ PQD/PDMS film. The encrypted information remained secure from unauthorized entities under both daylight and UV light, utilizing fake information until a predetermined time, after which the information leakage was furthered avoided with water immersion. Importantly, our encryption method necessitates only a UV light source and a trace amount of water for the entire decryption process. Given its cost-effectiveness and procedural simplicity, this investigation not only suggests the novel application of AEP as a straightforward and cost-effective surface defect passivation method for perovskite/polymer composites but also paves new avenues for these composites in the field of advanced information security.

CRediT authorship contribution statement

Jaehyeok Ryu: Writing – original draft, Conceptualization, Methodology, Investigation, Formal analysis, Data curation. **Jiyeon Lee:** Writing – review & editing, Resources, Data curation. **Dongjun Kim:** Investigation, Visualization. **Yu Jin Lee:** Investigation. **Ji Heon Kim:** Software. **Juwon Oh:** Validation, Funding acquisition. **Jiwon Kim:** Writing – review & editing, Validation, Supervision, Project administration, Funding acquisition.

Declaration of competing interest

The authors declare that they have no known competing financial interests or personal relationships that could have appeared to influence the work reported in this paper.

Acknowledgements

The work at Yonsei University was supported by the National Research Foundation of Korea (NRF) funded by the Korea Government (MSIT) (Nos. RS-2023-00240624 and RS-2025-00523354), and the work at Kyungpook National University was supported by the National Research Foundation of Korea (NRF) funded by the Korea Government (MSIT) (Nos. RS-2024-00343229 and RS-2024-00404760).

Appendix A. Supplementary data

Supplementary data to this article can be found online at https://doi.org/10.1016/j.nanoms.2025.03.004.

References

[1] A.O. Omoniyi, Y. Wang, S. Yang, J. Liu, J. Zhang, Z. Su, High-security information encryption strategy based on optical functional materials: a review on materials design, problems, multiple coding, and beyond, Mater, Today Commun. 36 (2023) 106508, https://doi.org/10.1016/j.mtcomm.2023.106508.

[2] Y. Ni, H. Wan, W. Liang, S. Zhang, X. Xu, L. Li, Y. Shao, S. Ruan, W. Zhang, Random lasing carbon dot fibers for multilevel anti-counterfeiting, Nanoscale 13 (2021) 16872–16878, https://doi.org/10.1039/D1NR04707H.

[3] S. Zhang, J. Wang, Y. Ni, Y. Li, H. Zhang, W. Zhang, Z. Xie, S. Zhou, Modulation of carbon dots hybrids lasers for high security flexible multi-level anti-counterfeiting, J. Alloys Compd. 957 (2023) 170307, https://doi.org/10.1016/j.jallcom.2023.170307.

[4] X.-F. Liu, L. Zou, C. Yang, W. Zhao, X.-Y. Li, B. Sun, C.-X. Hu, Y. Yu, Q. Wang, Q. Zhao, H.-L. Zhang, Fluorescence lifetime-tunable water-resistant perovskite quantum dots for multidimensional encryption, ACS Appl. Mater. Interfaces 12 (2020) 43073–43082, https://doi.org/10.1021/acsami.0c10869.

[5] J. Fu, J. Feng, B. Shi, Y. Zhou, C. Xue, M. Zhang, Y. Qi, W. Wen, J. Wu, Grading patterning perovskite nanocrystal-polymer composite films for robust multilevel information encryption and decryption, Chem. Eng. J. 451 (2023) 138240, https://doi.org/10.1016/j.cej.2022.138240.

[6] Y. Liu, Y. Zheng, Y. Zhu, F. Ma, X. Zheng, K. Yang, X. Zheng, Z. Xu, S. Ju, Y. Zheng, T. Guo, L. Qian, F. Li, Unclonable perovskite fluorescent dots with fingerprint

pattern for multilevel anticounterfeiting, ACS Appl. Mater. Interfaces 12 (2020) 39649–39656, https://doi.org/10.1021/acsami.0c11103.

[7] J.W. Oh, S. Lee, H. Han, O. Allam, J.I. Choi, H. Lee, W. Jiang, J. Jang, G. Kim, S. Mun, K. Lee, Y. Kim, J.W. Park, S. Lee, S.S. Jang, C. Park, Dual-light emitting 3D encryption with printable fluorescent-phosphorescent metal-organic frameworks, Light Sci. Appl. 12 (2023) 226, https://doi.org/10.1038/s41377-023-01274-4.

[8] W. Yang, L. Fei, F. Gao, W. Liu, H. Xu, L. Yang, Y. Liu, Thermal polymerization synthesis of CsPbBr3 perovskite-quantum-dots@copolymer composite: towards long-term stability and optical phosphor application, Chem. Eng. J. 387 (2020) 124180, https://doi.org/10.1016/j.cej.2020.124180.

[9] J. Wang, Z. Zhao, Y. Wu, C. Ye, Y. Zhang, Triple-modal anti-counterfeiting based on CsPbBr3 perovskite quantum dot/CaAl2O4:Eu2+, Nd3+ composites with dual fluorescence properties, ACS Appl. Nano Mater. 6 (2023) 10329–10339, https://doi.org/10.1021/acsanm.3c01253.

[10] X. Yu, K. Liu, H. Zhang, B. Wang, W. Ma, J. Li, J. Yu, Carbon dots-in-EuAPO-5 zeolite: triple-emission for multilevel luminescence anti-counterfeiting, Small 17 (2021) e2103374, https://doi.org/10.1002/smll.202103374.

[11] D. Gao, J. Gao, F. Gao, Q. Kuang, Y. Pan, Y. Chen, Z. Pan, Quintuple-mode dynamic anti-counterfeiting using multi-mode persistent phosphors, J. Mater. Chem. 9 (2021) 16634–16644, https://doi.org/10.1039/D1TC04568G.

[12] P. Feng, X. Yang, X. Feng, G. Zhao, X. Li, J. Cao, Y. Tang, C.-H. Yan, Highly stable perovskite quantum dots modified by europium complex for dual-responsive optical encoding, ACS Nano 15 (2021) 6266–6275, https://doi.org/10.1021/acsnano.0c09228.

[13] R. Gong, F. Wang, J. Cheng, Z. Wang, Y. Lu, J. Wang, H. Wang, Weak-solvent-modulated optical encryption based on perovskite nanocrystals/polymer composites, Chem. Eng. J. 446 (2022) 137212, https://doi.org/10.1016/j.cej.2022.137212.

[14] A. Dey, J. Ye, A. De, E. Debroye, S.K. Ha, E. Bladt, A.S. Kshirsagar, Z. Wang, J. Yin, Y. Wang, L.N. Quan, F. Yan, M. Gao, X. Li, J. Shamsi, T. Debnath, M. Cao, M.A. Scheel, S. Kumar, J.A. Steele, M. Gerhard, L. Chouhan, K. Xu, X.-G. Wu, Y. Li, Y. Zhang, A. Dutta, C. Han, I. Vincon, A.L. Rogach, A. Nag, A. Samanta, B.A. Korgel, C.-J. Shih, D.R. Gamelin, D.H. Son, H. Zeng, H. Zhong, H. Sun, H.V. Demir, I.G. Scheblykin, I. Mora-Seró, J.K. Stolarczyk, J.Z. Zhang, J. Feldmann, J. Hofkens, J.M. Luther, J. Pérez-Prieto, L. Li, L. Manna, M.I. Bodnarchuk, M.V. Kovalenko, M.B.J. Roeffaers, N. Pradhan, O.F. Mohammed, O.M. Bakr, P. Yang, P. Müller-Buschbaum, P.V. Kamat, Q. Bao, Q. Zhang, R. Krahne, R.E. Galian, S.D. Stranks, S. Bals, V. Biju, W.A. Tisdale, Y. Yan, R.L.Z. Hoye, L. Polavarapu, State of the art and prospects for halide perovskite nanocrystals, ACS Nano 15 (2021) 10775–10981, https://doi.org/10.1021/acsnano.0c08903.

[15] Y. Zhou, J. Chen, O.M. Bakr, H.-T. Sun, Metal-doped lead halide perovskites: synthesis, properties, and optoelectronic applications, Chem. Mater. 30 (2018) 6589–6613, https://doi.org/10.1021/acs.chemmater.8b02989.

[16] J. Kang, L.-W. Wang, High defect tolerance in lead halide perovskite CsPbBr3, J. Phys. Chem. Lett. 8 (2017) 489–493, https://doi.org/10.1021/acs.jpclett.6b02800.

[17] L. Protesescu, S. Yakunin, M.I. Bodnarchuk, F. Krieg, R. Caputo, C.H. Hendon, R.X. Yang, A. Walsh, M.V. Kovalenko, Nanocrystals of cesium lead halide perovskites (CsPbX3, X = Cl, Br, and I): novel optoelectronic materials showing bright emission with wide color gamut, Nano Lett. 15 (2015) 3692–3696, https://doi.org/10.1021/nl5048779.

[18] Y. Liu, Y. Zhang, Moving binary-color heterojunction for spatiotemporal multilevel encryption via directional swelling and anion exchange, ACS Nano 15 (2021) 7628–7637, https://doi.org/10.1021/acsnano.1c01180.

[19] Z. Wu, B. Du, G. Tong, H. Zhang, Y. Zhang, J. Xia, Z. Zhao, Highly luminescent and stable inorganic perovskite micro-nanocomposites for crucial information encryption and decryption, Chem. Eng. J. 428 (2022) 131016, https://doi.org/10.1016/j.cej.2021.131016.

[20] P.N. Rudd, J. Huang, Metal ions in halide perovskite materials and devices, Trends Chem. 1 (2019) 394–409, https://doi.org/10.1016/j.trechm.2019.04.010.

[21] R. Wang, J. Wang, S. Tan, Y. Duan, Z.-K. Wang, Y. Yang, Opportunities and challenges of lead-free perovskite optoelectronic devices, Trends Chem. 1 (2019) 368–379, https://doi.org/10.1016/j.trechm.2019.04.004.

[22] Z.-K. Wang, M. Li, Y.-G. Yang, Y. Hu, H. Ma, X.-Y. Gao, L.-S. Liao, High efficiency Pb-In binary metal perovskite solar cells, Adv. Mater. 28 (2016) 6695–6703, https://doi.org/10.1002/adma.201600626.

[23] S. Chen, X. Liu, Z. Wang, W. Li, X. Gu, J. Lin, T. Yang, X. Gao, A.K.K. Kyaw, Defect passivation of CsPbBr 3 with AgBr for high-performance all-inorganic perovskite solar cells, Adv. Energy Sustain. Res. 2 (2021) 2000099, https://doi.org/10.1002/aesr.202000099.

[24] S. Zhou, Y. Ma, G. Zhou, X. Xu, M. Qin, Y. Li, Y.-J. Hsu, H. Hu, G. Li, N. Zhao, J. Xu, X. Lu, Ag-doped halide perovskite nanocrystals for tunable band structure and efficient charge transport, ACS Energy Lett. 4 (2019) 534–541, https://doi.org/10.1021/acsenergylett.8b02478.

[25] S. Das Adhikari, A.K. Guria, N. Pradhan, Insights of doping and the photoluminescence properties of Mn-doped perovskite nanocrystals, J. Phys. Chem. Lett. 10 (2019) 2250–2257, https://doi.org/10.1021/acs.jpclett.9b00182.

[26] Y. Long, C. Wang, X. Liu, J. Wang, S. Fu, J. Zhang, Z. Hu, Y. Zhu, Zinc ion functional doping for all-inorganic planar CsPbIBr2 perovskite solar cells with efficiency over 10.5%, J. Mater. Chem. 9 (2021) 2145–2155, https://doi.org/10.1039/D0TC05455K.

[27] J. Ye, M.M. Byranvand, C.O. Martínez, R.L.Z. Hoye, M. Saliba, L. Polavarapu, Defect passivation in lead-Halide perovskite nanocrystals and thin films: toward efficient LEDs and solar cells, Angew. Chem. 133 (2021) 21804–21828, https://doi.org/10.1002/ange.202102360.

[28] M. Lu, X. Zhang, X. Bai, H. Wu, X. Shen, Y. Zhang, W. Zhang, W. Zheng, H. Song, W.W. Yu, A.L. Rogach, Spontaneous silver doping and surface passivation of CsPbI3 perovskite active layer enable light-emitting devices with an external quantum efficiency of 11.2%, ACS Energy Lett. 3 (2018) 1571–1577, https://doi.org/10.1021/acsenergylett.8b00835.

[29] J.W. Oh, H. Han, H.H. Kim, H. Lee, D. Kim, J. Lee, J. Kim, W.K. Choi, C. Park, Metal–organic framework-assisted metal-ion doping in all-inorganic perovskite for dual-mode image sensing display, Adv. Funct. Mater. 32 (2022) 2111894, https://doi.org/10.1002/adfm.202111894.

[30] F. Li, Y. Liu, H. Wang, Q. Zhan, Q. Liu, Z. Xia, Postsynthetic surface trap removal of CsPbX3 (X = Cl, Br, or I) quantum dots via a ZnX2/hexane solution toward an enhanced luminescence quantum yield, Chem. Mater. 30 (2018) 8546–8554, https://doi.org/10.1021/acs.chemmater.8b03442.

[31] M.C. Brennan, J.E. Herr, T.S. Nguyen-Beck, J. Zinna, S. Draguta, S. Rouvimov, J. Parkhill, M. Kuno, Origin of the size-dependent Stokes shift in CsPbBr3 perovskite nanocrystals, J. Am. Chem. Soc. 139 (2017) 12201–12208, https://doi.org/10.1021/jacs.7b05683.

[32] N. Fiuza-Maneiro, K. Sun, I. López-Fernández, S. Gómez-Graña, P. Müller-Buschbaum, L. Polavarapu, Ligand chemistry of inorganic lead halide perovskite nanocrystals, ACS Energy Lett. 8 (2023) 1152–1191, https://doi.org/10.1021/acsenergylett.2c02363.

[33] Y. Xin, H. Zhao, J. Zhang, Highly stable and luminescent perovskite–polymer composites from a convenient and universal strategy, ACS Appl. Mater. Interfaces 10 (2018) 4971–4980, https://doi.org/10.1021/acsami.7b16442.

[34] F. Boussoufi, M. Pousthomis, A. Kuntzmann, M. D'Amico, G. Patriarche, B. Dubertret, Spray-drying polymer encapsulation of CsPbBr3 perovskite nanocrystals with enhanced photostability for LED downconverters, ACS Appl. Nano Mater. 4 (2021) 7502–7512, https://doi.org/10.1021/acsanm.1c01552.

[35] Y. Li, L. Dong, N. Chen, Z. Guo, Y. Lv, J. Zheng, C. Chen, Room-temperature synthesis of two-dimensional hexagonal boron nitride nanosheet-stabilized CsPbBr3 perovskite quantum dots, ACS Appl. Mater. Interfaces 11 (2019) 8242–8249, https://doi.org/10.1021/acsami.8b20400.

[36] T. Xuan, J. Huang, H. Liu, S. Lou, L. Cao, W. Gan, R.-S. Liu, J. Wang, Super-hydrophobic cesium lead Halide perovskite quantum dot-polymer composites with high stability and luminescent efficiency for wide color gamut white light-emitting diodes, Chem. Mater. 31 (2019) 1042–1047, https://doi.org/10.1021/acs.chemmater.8b04596.

[37] M. Kafetzi, S. Pispas, G. Mousdis, Hybrid perovskite/polymer materials: preparation and physicochemical properties, J. Compos. Sci. 5 (2021) 304, https://doi.org/10.3390/jcs5110304.

[38] S.M.H. Qaid, H.M. Ghaithan, B.A. Al-Asbahi, A.S. Aldwayyan, Ultra-stable polycrystalline CsPbBr3 perovskite–polymer composite thin disk for light-emitting applications, Nanomaterials 10 (2020) 2382, https://doi.org/10.3390/nano10122382.

[39] C.-H. Sung, S.-D. Huang, G. Kumar, W.-C. Lin, C.-C. Lin, H.-C. Kuo, F.-C. Chen, Highly luminescent perovskite quantum dots for light-emitting devices: photopatternable perovskite quantum dot–polymer nanocomposites, J. Mater. Chem. 10 (2022) 15941–15947, https://doi.org/10.1039/D2TC01832B.

[40] L.M. Johnson, L. Gao, C.W. Shields IV, M. Smith, K. Efimenko, K. Cushing, J. Genzer, G.P. López, Elastomeric microparticles for acoustic mediated bioseparations, J. Nanobiotechnol. 11 (2013) 22, https://doi.org/10.1186/1477-3155-11-22.

[41] J. Lee, J. Kim, H. Kim, Y.M. Bae, K.-H. Lee, H.J. Cho, Effect of thermal treatment on the chemical resistance of polydimethylsiloxane for microfluidic devices, J. Micromech. Microeng. 23 (2013) 035007, https://doi.org/10.1088/0960-1317/23/3/035007.

[42] N.K. Sethy, Z. Arif, P.K. Mishra, P. Kumar, Nanocomposite film with green synthesized TiO2 nanoparticles and hydrophobic polydimethylsiloxane polymer: synthesis, characterization, and antibacterial test, J. Polym. Eng. 40 (2020) 211–220, https://doi.org/10.1515/polyeng-2019-0257.

[43] R. Prasanna, A. Gold-Parker, T. Leijtens, B. Conings, A. Babayigit, H.-G. Boyen, M.F. Toney, M.D. McGehee, Band gap tuning via lattice contraction and octahedral tilting in perovskite materials for photovoltaics, J. Am. Chem. Soc. 138 (2017) 11117–11124, https://doi.org/10.1021/jacs.7b04981.

[44] D. Amgar, T. Binyamin, V. Uvarov, L. Etgar, Near ultra-violet to mid-visible band gap tuning of mixed cation RbxCs1−xPbX3 (X = Cl or Br) perovskite nanoparticles, Nanoscale 10 (2018) 6060–6068, https://doi.org/10.1039/C7NR09607K.

[45] J. Meng, Z. Lan, M. Abdellah, B. Yang, S. Mossin, M. Naumova, Q. Shi, S.L.G. Alvarez, Y. Liu, W. Lin, I.E. Castelli, S.E. Canton, T. Pullerits, K. Zheng, Modulating charge-carrier dynamics in Mn-doped all-inorganic halide perovskite quantum dots through the doping-induced deep trap states, J. Phys. Chem. Lett. 11 (2020) 3705–3711, https://doi.org/10.1021/acs.jpclett.0c01050.

[46] Z. Gong, W. Zhang, S. Pan, J. Pan, Ag^{+}/Bi^{3+} doping induced band structure and optoelectronic properties changes in $CsPbBr_3$ crystals, J. Cryst. Growth 586 (2022) 126604, https://doi.org/10.1016/j.jcrysgro.2022.126604.

[47] J. Cao, S.X. Tao, P.A. Bobbert, C.-P. Wong, N. Zhao, Interstitial occupancy by extrinsic alkali cations in perovskites and its impact on ion migration, Adv. Mater. 30 (2018) e1707350, https://doi.org/10.1002/adma.201707350.

[48] Y. Xie, B. Peng, I. Bravić, Y. Yu, Y. Dong, R. Liang, Q. Ou, B. Monserrat, S. Zhang, Highly efficient blue-emitting $CsPbBr_3$ perovskite nanocrystals through neodymium doping, Adv. Sci. 7 (2020) 2001698, https://doi.org/10.1002/advs.202001698.

[49] C. Park, S.J. Yang, J. Choi, S. Song, W. Choi, K. Cho, Improved chemical stability of organometal halide perovskite solar cells against moisture and heat by Ag doping, ChemSusChem 13 (2020) 3261–3268, https://doi.org/10.1002/cssc.202000192.

[50] X. Yuan, X. Hou, J. Li, C. Qu, W. Zhang, J. Zhao, H. Li, Thermal degradation of luminescence in inorganic perovskite CsPbBr3 nanocrystals, Phys. Chem. Chem. Phys. 19 (2017) 8934–8940, https://doi.org/10.1039/C6CP08824D.

[51] X. Lü, W. Yang, Q. Jia, H. Xu, Pressure-induced dramatic changes in organic–inorganic halide perovskites, Chem. Sci. 8 (2017) 6764–6776, https://doi.org/10.1039/C7SC01845B.

[52] C.E. Rowland, I. Fedin, H. Zhang, S.K. Gray, A.O. Govorov, D.V. Talapin, R.D. Schaller, Picosecond energy transfer and multiexciton transfer outpaces Auger recombination in binary CdSe nanoplatelet solids, Nat. Mater. 14 (2015) 484–489, https://doi.org/10.1038/nmat4231.

[53] T. Kim, S.I. Jung, S. Ham, H. Chung, D. Kim, Elucidation of photoluminescence blinking mechanism and multiexciton dynamics in hybrid organic-inorganic perovskite quantum dots, Small 15 (2019) e1900355, https://doi.org/10.1002/smll.201900355.

[54] G.S. Offeddu, L. Mohee, R.E. Cameron, Scale and structure dependent solute diffusivity within microporous tissue engineering scaffolds, J. Mater. Sci. Mater. Med. 31 (2020) 46, https://doi.org/10.1007/s10856-020-06381-x.

[55] D.J. Wolak, M.E. Pizzo, R.G. Thorne, Probing the extracellular diffusion of antibodies in brain using in vivo integrative optical imaging and ex vivo fluorescence imaging, J. Contr. Release 197 (2015) 78–86, https://doi.org/10.1016/j.jconrel.2014.10.034.

[56] J. Grant, A. Özkan, C. Oh, G. Mahajan, R. Prantil-Baun, D.E. Ingber, Simulating drug concentrations in PDMS microfluidic organ chips, Lab Chip 21 (2021) 3509–3519, https://doi.org/10.1039/d1lc00348h.

[57] R. Jakieła, A. Barcz, E. Wegner, A. Zagojski, Diffusion of Mn in gallium arsenide, J. Alloys Compd. 423 (2006) 132–135, https://doi.org/10.1016/j.jallcom.2005.12.053.

[58] S. Cheng, H. Zhong, What happens when halide perovskites meet with water? J. Phys. Chem. Lett. 13 (2022) 2281–2290, https://doi.org/10.1021/acs.jpclett.2c00166.

[59] C.C. Boyd, R. Cheacharoen, T. Leijtens, M.D. McGehee, Understanding degradation mechanisms and improving stability of perovskite photovoltaics, Chem. Rev. 119 (2019) 3418–3451, https://doi.org/10.1021/acs.chemrev.8b00336.

[60] K. Kim, D.J. Siegel, Correlating lattice distortions, ion migration barriers, and stability in solid electrolytes, J. Mater. Chem. A 7 (2019) 3216–3227, https://doi.org/10.1039/C8TA10989C.

[61] D. Kim, T. Yun, S. An, C.-L. Lee, How to improve the structural stabilities of halide perovskite quantum dots: review of various strategies to enhance the structural stabilities of halide perovskite quantum dots, Nano Convergence 11 (2024), https://doi.org/10.1186/s40580-024-00412-x.

[62] Y.-Y. Wang, X. Song, S. Liu, G.-R. Li, S.-H. Ye, X.-P. Gao, Elucidating the effect of the dopant ionic radius on the structure and electrochemical performance of Ni-rich layered oxides for lithium-ion batteries, ACS Appl. Mater. Interfaces 13 (2021) 56233–56241, https://doi.org/10.1021/acsami.1c17991.

[63] Y. Li, Q.-L. Li, Y. Li, Y.-L. Yang, S.-L. Zhang, J. Zhao, J. Wan, Z. Zhang, Water-assistant ultrahigh fluorescence enhancement in perovskite polymer-encapsulated film for flexible X-ray scintillators, Chem. Eng. J. 452 (2023) 139132, https://doi.org/10.1016/j.cej.2022.139132.